Novel Applications of Super-Resolution Microscopy in Molecular Biology and Medical Diagnostics

Dissertation

in partial fulfillment of the requirements for the degree

“Doctor of Natural Sciences (Doctor rerum naturalium)”

of the Georg August University Göttingen

within the doctoral program Molecular Physiology of the Brain

submitted by

WILLIAM I. ZHANG

born in

GÖTTINGEN, GERMANY

Göttingen, September 2015

Novel Applications of Super-Resolution Microscopy in Molecular Biology and Medical Diagnostics

Dissertation

in partial fulfillment of the requirements for the degree

“Doctor of Natural Sciences (Doctor rerum naturalium)”

of the Georg August University Göttingen

within the doctoral program Molecular Physiology of the Brain

submitted by

WILLIAM I. ZHANG

born in

GÖTTINGEN, GERMANY

Göttingen, September 2015

THESIS COMMITTEE

Prof. Dr. Silvio O. Rizzoli; Dept. of Neuro- & Sensory Physiology, University Medical Center, Göttingen, Germany

Prof. Dr. Tiago Outeiro; Dept. of Neurodegeneration and Restorative Research, University Medical Center, Göttingen, Germany

Prof. Dr. Gerhard Braus; Institute for Microbiology and Genetics, University of Göttingen, Göttingen, Germany

MEMBERS OF THE EXAMINATION BOARD

1st referee
Prof. Dr. med. Anja Schneider, Translational Dementia Research, German Center for Neurodegenerative Diseases (DZNE) within the Helmholtz Association, Dept. of Psychiatry and Psychotherapy, University Medical Center, Göttingen, Germany

2nd referee
Prof. Dr. Stefan Jakobs; Dept. of NanoBiophotonics, Mitochondrial Structure and Dynamics, Max-Planck-Institute for Biophysical Chemistry, Göttingen, Germany

3rd referee
Prof. Dr. Paul Lingor; Dept. of Neurology, University Medical Center, Göttingen, Germany

Date of thesis defense: *18th November 2015*

I hereby declare that I prepared this dissertation independently and with no other sources and aids than quoted.

Göttingen, 30th September 2015

S ***tudy***

C ***reativity***

I ***nnovation***

E ***nthusiasm***

N ***etwork***

C ***ourage***

E ***ndurance***

Table of contents

List of Publications

Lewis MA, Buniello A, Hilton JM, Zhu F, **Zhang WI**, Evans S, van Dongen S, Enright A, Steel KP (2016) Exploring regulatory networks of miR-96 in the developing inner ear. *Sci Rep, accepted.*

Zhang WI, Antonios G, Rabano A, Bayer TA, Schneider A, Rizzoli SO (2015) Super-resolution microscopy of CSF biomarkers as a tool for Alzheimer's disease diagnostics. *J Alzheimer Dis, epub 2015 Apr 15.*

Zhang WI, Röhse H, Rizzoli SO, Opazo F (2014) Fluorescent in situ hybridization of synaptic proteins imaged with super-resolution STED microscopy. *Microsc Res Tech 77, 517-527.*

Acknowledgements

First and foremost, I would like to thank Silvio Rizzoli from the bottom of my heart. He was not only my PI who guided me scientifically, I can honestly say that he has been my mentor. Without his support, I would not be where I am now.

I also would like to thank my thesis committee members Anja Schneider, Tiago Outeiro, and Gerhard Braus for their support during the PhD project, providing scientific input and encouragement throughout the doctorate; and Stefan Jakobs and Paul Lingor, for being part of the extended committee.

Personal thanks go to everyone who supported me during this very dynamic phase of my life. You know who you are and I sincerely thank you more than words can say.

List of media

List of abbreviations

Aβ	β-amyloid
AD	Alzheimer's disease
APD	avalanche photo diode
APP	amyloid precursor protein
bp	base pairs
CCD	charge-coupled device
CDS	coding sequence
ciRNA	circular RNA
CSF	cerebrospinal fluid
DNA	deoxyribonucleic acid
(F)ISH	(fluorescence) *in situ* hybridization
HFIP	1,1,1,3,3,3-hexafluoro-2-propanol
HMW	high molecular weight
LMW	low molecular weight
lncRNA	long non-coding RNA
MCI	mild cognitive impaired
miRNA	micro RNA
mRNA	messenger RNA
NaCl	sodium chloride
NaOH	sodium hydroxide
n.s.	not significant
PALM	photo-activated localization microscopy
PMT	photo multiplier tube
qPCR	quantitative polymerase chain reaction
RNA	ribonucleic acid
SEC	size-exclusion chromatography
STED	stimulated emission depletion
STORM	stochastic optical reconstruction microscopy
Stg	synaptotagmin
Syp	synaptophysin
TIRF	total internal reflection fluorescence

Tm	melting temperature
tRNA	transfer RNA
UTR	untranslated region
UV	ultra violet
VAMP	synaptobrevin

Abstract

Despite recent advances in microscopy techniques, the underlying labeling assays remained mostly unchanged. However, super-resolution techniques require other staining conditions than conventional light microscopy, like more dense labeling, which is not always trivial to achieve. In this work, I present two novel applications of stimulated emission depletion (STED) microscopy to the fields of molecular biology and medical diagnostics. For one, I established a fluorescent *in situ* hybridization (FISH) protocol to investigate mRNAs of the three synaptic proteins synaptophysin, synaptobrevin, and synaptotagmin in primary hippocampal neurons. This achieved more precise information regarding the mRNA numbers and organization than conventional confocal microscopy. Secondly, I applied STED microscopy for the development of a novel diagnosis method for Alzheimer's disease (AD). The increased resolution was sufficiently high to discriminate low and high molecular weight β-amyloid (Aβ) aggregates produced *in vitro*. Analysis of cerebrospinal fluid (CSF) samples from 36 AD patients, 11 patients with mild cognitive impairment (MCI), and 21 controls allowed a separation of AD patients from controls with ~87% specificity and ~79% sensitivity. In conclusion, this work illustrates the need for optimization of long established methods depending on the imaging technique and sample to obtain more accurate data.

1. Introduction

1.1. A brief history of microscopy and imaging

Throughout history, there has always been a fascination about what the world is composed of. However, the human eye can only distinguish two elements if they are at least 0.1 mm apart, therefore having a spatial resolution of 0.1 mm (Alberts, 2014). In order to see smaller objects, optical tools have been developed, like magnifying glasses or microscopes. Anton van Leeuwenhoek could be considered as the inventor of the first compound microscope with a sophisticated optical apparatus in the 17th century (Baker, 1739). The first microscopes allowed the investigation of biological samples at unprecedented detail. For example, van Leeuwenhoek discovered spermatozoa and Robert Hooke described the first plant cells (Hooke, 1665, Baker, 1739).

The reason why the sample can be seen under this type of microscopes, bright-field microscopes, is based on varying light scattering and absorption properties of the sample that result in contrast differences. However, most biological samples have only low contrast rendering detailed observations difficult. Staining procedures change the optophysical properties of parts of the sample, thereby increasing the contrast. A famous example would be the silver staining invented by Camillo Golgi in 1873 (Golgi, 1873). This technique introduces silver precipitate into the sample which then appear black in brightfield due to the high light absorption. By highlighting only specific parts, the composition of the sample could be investigated more accurately.

Ramón y Cajal used Golgi's method that had been around for several years and adapted the staining procedure according to the sample (Ramón y Cajal, 1917). This allowed him to draw his observations in extensive detail. His sketches of Purkinje cells, in particular, are famous. His findings contributed majorly to the knowledge about neuron structure and the cell as elementary component of complex organisms. Ramón y Cajal's findings are a valuable example of how an established method can be improved to obtain new data.

Based on the same principle of restricting the detection to specific parts of the sample, fluorescence microscopy became a milestone in the microscopy field. Instead of white light, which consists of a mixture of light with different wavelengths, fluorescence microscopy uses only parts of the spectrum. This light is absorbed by a fluorescent dye and light with less energy, i.e. at a longer wavelength, is emitted and detected. This results in the maximum contrast by limiting the signal to the location of the staining, while the rest of the sample remains mostly undetected. Another

advantage of using light from only parts of the spectrum is the improvement of the optical resolution. In 1873, Ernst Abbe published an equation describing the resolution limit of microscopes in relation to the wavelength of light used or light detected, respectively (Equation I; Abbe, 1873). Using only a narrow part of the spectrum therefore reduces the blurriness due to diffraction and increasesb the resolution of the system.

$$d = \frac{\lambda}{2n \cdot \sin(\theta)} = \frac{\lambda}{2 \cdot NA}$$

(I) Equation | Abbe's equation of diffraction limit. This equation describes the theoretical resolution limit of optical systems, where λ is the wavelength of light passing through the lens, n is the refractive index of the medium the light is traveling through, and θ is the angle the light is entering the lens with.

Fluorescence microscopy requires specific staining methods to introduce the fluorescent dye into the sample. This can be achieved, similar to the silver staining, based on the biophysical properties like hydrophobicity. Another approach would be to label proteins of interest specifically with so-called affinity probes. Affinity probes are molecules that specifically bind to another target molecules non-covalently to enable their detection. The most common technique of the latter approach is immunostaining, which uses fluorescently labeled antibodies.

Confocal microscopes show an even higher resolution based on the same principle to reduce the signal to a very defined and restricted area. A confocal microscope is a fluorescence microscope illuminating only small parts of the sample at a given time. Additionally, it contains a diaphragm, the so-called pinhole, that excludes light from outside the focal plane (z-plane). The improved resolution of confocal microscopes has been used to investigate what cells are comprised of and how the cell functions. Therefore, it is understandable that increased resolution offers a more accurate representation of the cell.

The electron microscope achieves even higher resolutions by substituting light with electrons. The beam of electrons has a shorter wavelength than UV light, within the picometer range (Erni, 2009). However, using electrons requires preparation of the sample under harsh conditions. This procedure is laborious, requires fixation of the sample, and is prone to introduce artifacts (Tapia et al., 2012). Specific labeling of target proteins is rather difficult which makes - despite the inferior resolution - fluorescence microscopy more versatile and therefore the method of choice for this work.

1.2. A recent milestone in fluorescent microscopy: nanoscopy

During the past decades, innovations in the field of fluorescence microscopy have managed to circumvent Abbe's diffraction limit. The field of nanoscopy, also named super-resolution microscopy, emerged. The Nobel prize for Chemistry was recently awarded to two of those novel techniques: first, stimulated emission depletion (STED) microscopy by Stefan W. Hell. It reduces the signal to a confined area by application of Albert Einstein's eponymous theory of stimulated depletion (Willig et al., 2006). The principle of stimulated depletion uses photons to stimulate excited electrons of the illuminated fluorophores to fall back to ground state. This results in light emission with the same wavelength as the photons used for de-excitation which can be excluded from detection by filters (Einstein, 1916). This so-called STED effect is applied to the periphery of the diffraction limited fluorescent spot (Figure 1, blue) by superimposing a second, donut-shaped laser beam (red). This allows the detection of only the center of the excited spot, where the power of the STED beam is close to zero (yellow) since the STED laser de-excites fluorophores in relation to its power. The lasers scan, i.e. are moved across the sample, to create the image.

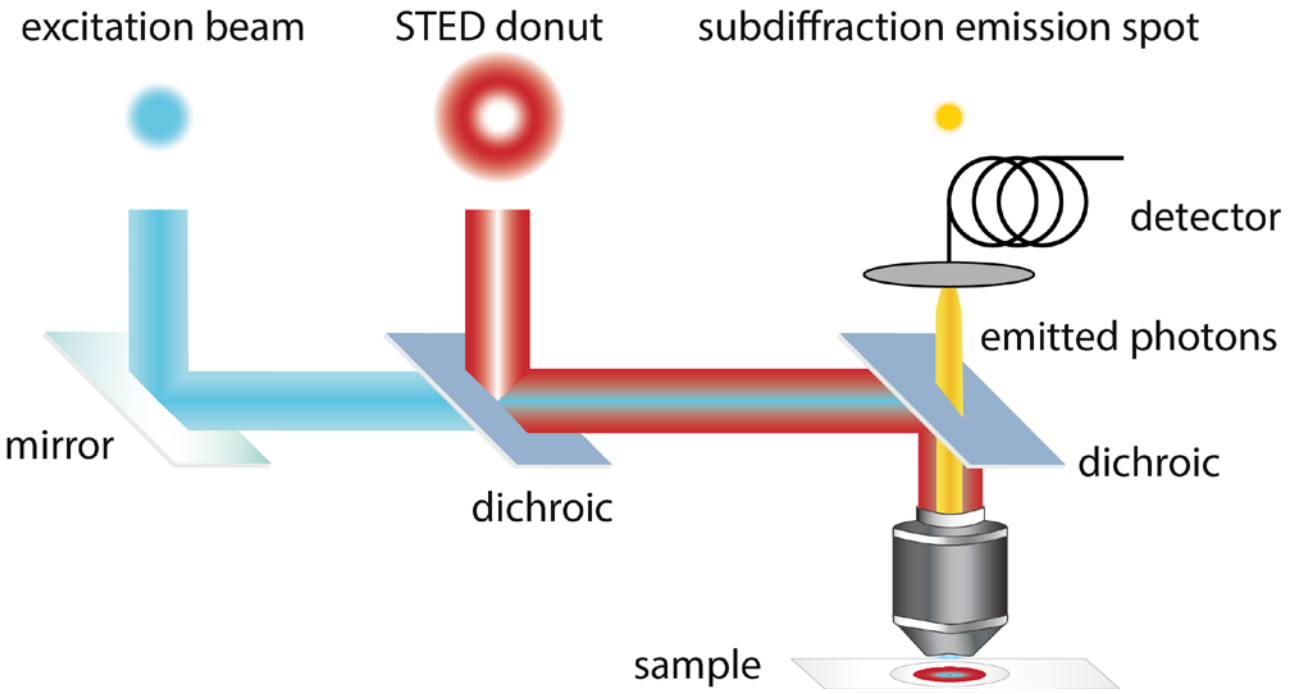

(1) Figure | Schematic overview of the functionality of STED. The sample is excited by a laser (cyan) like in a conventional laser scanning microscope. It is followed by a slightly delayed second laser (red) modulated to the shape of a toroid for de-exciting the previously excited fluorophores. Only the fluorophores in the center of the toroid, where the laser intensity is close to zero, will emit light and thereby creating a subdiffractional spot (yellow).

Higher intensities correlate with more de-excitation resulting in a smaller focal spot and higher resolution, making STED theoretically not limited to a physical barrier (Equation II). STED microscopy has been used on samples which require high spatial resolution, such as investigation of densely labeled protein clusters in the plasma membrane (Hoopmann et al. 2010; Opazo et al 2010; Sieber et al 2007).

$$d_{x,y} = \frac{\lambda}{2n \cdot sin(\theta) \cdot \sqrt{1 + \frac{I}{I_{sat}}}}$$

(II) Equation | Lateral resolution of STED microscopy. This equation describes the theoretical resolution limit of optical systems, where λ is the wavelength of light, n is the refractive index of the medium, θ is the angle the light is entering with, I is the focal intensity, and I_{sat} is the saturation intensity, which describes the value at which the fluorescence is reduced to half. Since λ, n, and θ are constants, the lateral resolution is only determined by I/I_{sat} and therefore independent of diffraction.

The second super-resolution principle credited by the 2014 chemistry Nobel prize concerns the detection of the fluorophores in a temporally separated manner rather than in a spatial configuration (Betzig, 2006, Moerner, 2006). Stochastic optical reconstruction microscopy (STORM) exploits the inherent blinking nature of the fluorophores, i.e. fluorescence emission is a stochastic event, while photo-activated localization microscopy (PALM) uses light to switch photo-activatable fluorophores on and off. This allows image acquisition of fluorophore subpopulations at a given time. The diffraction limited spots are likely to be separated further than the diffraction limit and can therefore be located with high precision. A series of images is then used to reconstruct an diffraction unlimited image (reviewed in Toomre and Bewersdorf, 2010). The advantage of PALM/STORM is the simple set up. Both techniques are based on epifluorescence/TIRF microscopes and can be used with a variety of fluorescent dyes. On the other hand, using chip-based detection systems requires a high labeling density due to the inferior sensitivity compared to photon-counting systems, like photo multiplier tubes (PMTs) or avalanche photo diodes (APDs) commonly used for STED microscopy.

1.3. Nanoscopy in molecular biology: RNA research

A prominent example of densely labeled structures, where super-resolution is needed, are RNAs. The importance of RNA spikes upon the identification of new RNA species with unidentified function. In the 1950-60s, an intermediate between DNA and protein has been identified, the

messenger RNA (mRNA) (Jacob, 1961). Around the same time, it was found that ribosomes contain RNA as essential component for translation, which in turn is a process relying on another type of RNA: transfer RNA (tRNA) (Hoagland, 1956). tRNAs are triplets of RNA nucleotides encoding for the different amino acids.

Since the 1990s, several RNA species where identified that do not code for proteins, summarized as non-coding RNAs. One representative are miRNAs, short RNA sequences that regulate protein expression post-transcriptionally (Bartel, 2004). Some miRNAs have been associated with diseases (e.g. Lewis and Steel, 2010), other non-coding RNAs have been discovered recently but their function is still unknown (long non-coding RNAs, lncRNAs; circular RNAs, ciRNAs) (Kapranov et al., 2007, Ebbesen et al., 2015).

Biochemical and PCR-based methods (including sequencing) provide information about their biochemical properties and sequence but are rather limited concerning identification of function. The above mentioned approaches have the disadvantage requiring destruction of the cell. However, the location of the investigated molecule within the intact cell can provide valuable information about its function. Therefore, an imaging based technique for the investigation of RNAs would be desirable. *In situ* hybridization (ISH) is a method that visualizes nucleic acids (DNA or RNA) by exploiting their intrinsic hybridization properties of the base pairing (guanine:cytosine, adenine:thymine, and adenine:uracil). Labeled DNA or RNA sequences (probes) that are reverse complementary to the target sequence are introduced into the cell. These probes act as affinity probes and hybridize specifically to the target sequence and can then be detected directly or indirectly. The label can be detected directly if it contains a fluorophore (fluorescent *in situ* hybridization, FISH) or indirectly, which detection requires additional steps like immunostaining (Figure 2), thereby increasing the spot size. Many mRNAs are expressed abundantly in the cytosol, i.e. show a high labeling density. This makes identification of individual RNA molecules difficult, which is exacerbated by diffraction limited imaging techniques. In theory, a FISH protocol using directly labeled probes for super-resolution microscopy should be able to address those issues.

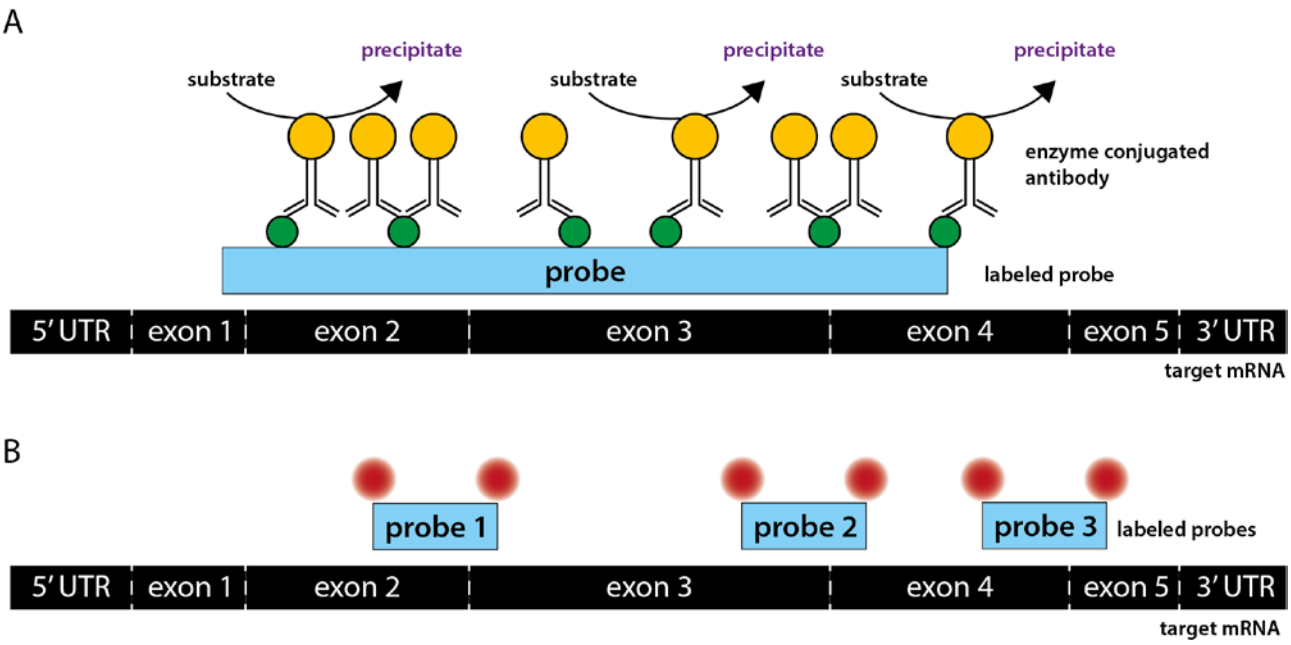

(2) Figure | Principle of ISH. (A) RNA probes (cyan) are produced *in vitro* with randomly inserted labeled nucleotides, e.g. digoxigenin (DIG, green). The label is detected by enzyme-linked antibodies (yellow) which catalyze a reaction to form a colored precipitate. (B) Multiple synthetical DNA probes (cyan) with a defined number of fluorophores at a defined location within the probe (red) can be detected by fluorescence microscopy.

1.4. Nanoscopy in medicine: AD research

[For text related to the medical part of this work, I may refer to Aβ peptides as proteins for readability, especially in conjunction with tau protein.]

Increased resolution is not only required for investigations of densely labeled samples but also when the size of the target of interest is relevant. One example in the field of medicine would be protein aggregates observed in Alzheimer's disease (AD).

AD is the most common form of dementia and was first described by Alois Alzheimer in 1907 as a "peculiar disease of the cerebral cortex" (Alzheimer, 1907). The reported female patient showed severe memory deficits and disorientation, while her motor ability remained normal. After her death, the autopsy revealed abnormal intracellular fibrils and macroscopic plaques in the cortex. Alzheimer made those neurofibrillary tangles and amyloid plaques, which became the neuropathological hallmarks of AD, responsible for the degeneration of neurons.

This correlation was established more than 60 years later upon the work of Blessed, Tomlinson, and Roth (Blessed, 1968). The authors investigated post-mortem brain samples with respect to the patients' cognitive capabilities before death. They found that the number plaques correlates with

dementia severity. Another 15 years later, it was found that those amyloid fibrils and neurofibrillary tangles consist mainly of β-amyloid (Aβ) and hyperphosphorylated tau, respectively (Glenner and Wong, 1984, Dickson, 1992, Morris et al., 2011).

The amyloid precursor protein (APP) is a transmembrane protein (Figure 3). It has been related to several functions, including synapse formation and function (Priller et al., 2006), neural plasticity (Turner et al., 2003), and iron metabolism (Duce et al., 2010). Mutations of APP have been associated with abnormally elevated levels of its cleavage product Aβ causing familial cases of AD (e.g. Scheuner et al., 1996). Aβ is released to the extracellular space upon two successive cleavages of β- (orange) and γ-secretase (green), where it aggregates to oligomers and eventually insoluble fibrils (lower part). APP can also be processed by a non-amyloidogenic pathway, where α-secretase (red) cleaves APP within the Aβ sequence (dashed box). However, the functions of both APP and its cleavage products are still unclear and under active investigation.

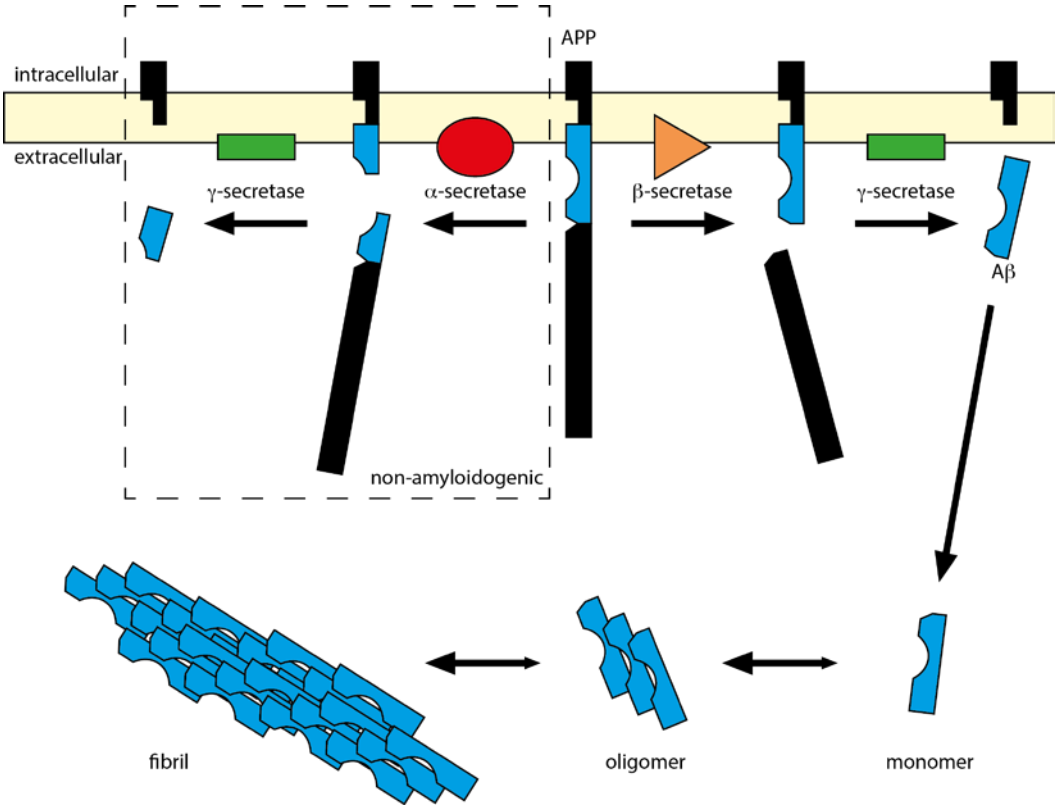

(3) Figure | Proteolytic processing of APP and formation of plaques. The transmembrane protein APP can be processed in two ways: 1) In the non-amyloidogenic pathway (dashed box): α-secretase (red) cleaves APP within the Aβ sequence (cyan) which prevents release of Aβ upon subsequent cleavage of γ-secretase (green). 2) The amyloidogenic pathway: if APP is processed by β-secretase (orange) prior to γ-secretase, Aβ is released into the extracellular space and can form oligomers and fibrils.

However, even after more than a century of research, it is still under debate if those macroscopic assemblies, i.e. amyloid plaques and neurofibrillary tangles, are indeed causing neurotoxicity in AD. There are several reports of patients with AD symptoms but no plaques or tangles, as well as individuals with plaques or tangles but no signs of dementia (e.g. Terry et al., 1991). But it has been rather well established that Aβ and tau play a central role in AD pathology. This led to the hypothesis that smaller, soluble assemblies may be the actual toxic forms rather than large, insoluble ones (Viola and Klein, 2015). It is thought that formation of those aggregates may even be a cellular response to counteract the neurotoxicity by sequestering the toxic oligomers in those insoluble deposits. Various studies used a range of techniques trying to identify the toxic species. Different synthetic Aβ species have been investigated *in vitro or* applied to various cell and animal models to mimic the disease with varying results (Motter, 1995, Georganopoulou et al., 2005, Esparza et al., 2013, Savage et al., 2014).

1.4.1. Current state of AD diagnosis

Autopsy is currently still the definite determination of AD. Pre-mortem, the diagnosis of AD is still mainly based on cognitive tests which are performed oftentimes over years and require experienced neurologists (McKhann et al., 2011). Therefore, an alternative diagnosis method is actively searched for that relies on lab results. Currently, the most promising lab-based diagnosis method relies on enzyme-linked immunosorbent assay (ELISA). The protein of interest, Aβ and tau are most commonly used, is immobilized and its concentration is measured using enzyme-linked antibodies. Those enzymes catalyze a chemical reaction that emits light (bioluminescence), which is used to extrapolate the amount of antibodies and therefore the amount of the protein of interest.

Due to their easy accessibility, serum and blood have been used as sample. However, the results are inconclusive (Mayeux et al., 2003, Irizarry, 2004, van Oijen et al., 2006), therefore making cerebral spinal fluid (CSF) the sample of choice. CSF surrounds the central nervous system where it mediates the exchange of metabolites between the central nervous system and the blood circulatory system. Since amyloid plaques are found extracellularly, there is a high chance that the composition of CSF reflects the situation in the brain and therefore can be used as a way to monitor AD development and progression.

Despite promising studies of ELISA using CSF, their results are still under debate (McKhann et al., 2011, Zetterberg and Blennow, 2013). An assay that relies not only on total protein concentrations but also factors in assembly size and structure (i.e. fibrillar, spherical, etc.) should be more precise

and thus more promising for a new diagnosis method (Fukumoto et al., 2010). In theory, imaging immunostained CSF at high resolution should be able to provide this type of data.

1.5. Scope of this work

In this study, I optimized established staining methods in the fields of molecular biology and medical diagnosis for STED microscopy, i.e. fluorescent *in situ* hybridization (FISH) and immunostaining, respectively. Regarding the former, STED-FISH may shed new light on past issues or provide valuable information on current ones, e.g. on the recently identified circular RNAs (ciRNAs) to help unveiling their function. Imaging methods like FISH may identify or at least exclude functions due to (co-)localization data. Due to the high density of RNAs within cells, the resolution of conventional light microscopy is not sufficient to obtain accurate information about the organization of RNAs. Therefore, I optimized a FISH protocol for STED microscopy to contribute to the investigation of the molecular mechanisms of mRNA distribution and dynamics within cells.

Concerning the field of medical diagnosis, super-resolution - based techniques may contribute to the research on aggregopathies like Alzheimer's disease (AD). Despite decades of research, neither is the exact cause known, nor does a successful therapy exist. The two candidate proteins Aβ and tau have been used as biomarker to develop a diagnosis method, mostly based on ELISA with varying results. There is a need for a reliable, lab-based diagnosis method which, ideally, fulfill all these features: 1) it should be lab-based, i.e. independent from the person doing the experiment; and yield immediate results unlike cognitive tests which may take several years. 2) it should also be able to monitor disease severity since different disease stages might require different treatment. 3) It should be able to predict the disease at prodromal stages, where the patients are still symptom free. Based on those requirements, I approached this problem from a more direct angle. Instead of relying on assays which only determine the concentrations or use rather harsh conditions to investigate those fragile assemblies, I wanted to monitor Aβ and tau particles directly. In principle, this should be feasible by immunostaining and fluorescence microscopy. However, those assemblies are smaller than the diffraction limit of conventional (confocal) light microscopy (~200 nm). This is why I turned to STED microscopy, which has a resolution limit of ~50 nm at our microscope. I tried to develop a diagnosis method using super-resolution imaging data of immunostained Aβ and tau in CSF. The STED parameters spot size, spot number, spot intensity, total fluorescence intensity should, in principle, reflect dimensions of the particles, number of particles, how many Aβ or tau

molecules per particle, and overall protein concentration, respectively. These features then can be used to possibly discriminate AD patients and controls.

2. Results

2.1. Establishing a FISH protocol for STED microscopy

Super-resolution microscopy has been mostly applied to studies of protein organization with regard to biological samples. Not only the number of studies identifying new RNA species but also their role in regulating protein expression has been increasing. However, those studies mostly relied on sequencing or biochemical assays. In this work, I refined the fluorescent *in situ* hybridization (FISH) protocol for STED microscopy I established during my Master's thesis (Zhang, 2011). This does not only allow to localize RNAs but also to monitor their intermolecular organization.

For this approach, I chose to use fluorescently labeled DNA oligonucleotides as probes for the following reasons: 1) DNA probes are easier to handle due to widespread presence of RNases, thereby reducing the risk of degradation of the probes and signal loss. 2) Short probes penetrate cells and tissue easier than long ones. 3) Short probes also enable the use of multiple different probes per target RNA to increase the signal-to-noise ratio. 4) Since the probes are chemically synthesized, the probes have a defined number of fluorophores at defined positions rather than random incorporation of labeled nucleotides during *in vitro* transcription.

2.1.1. STED-FISH stains mRNAs specifically

To check whether the FISH staining was specific, two control experiments were performed. First, cells that do not express the three synaptic proteins synaptophysin, synaptobrevin, and synaptotagmin endogenously were transfected to express the synaptic proteins and stained by FISH. Second, the same mRNAs of the three synaptic proteins were stained by FISH by three different probes, this time not covering the coding sequences (CDSs) but the untranslated regions (UTRs).

Regarding the first control experiment, the transfected cells can be easily identified because they express the synaptic protein fused to a GFP derivate called pHlourin (Figure 4, green). FISH signal could be observed in transfected cells only (Figure 4 B, red). Little signal could be detected in transfected cells using the control probes. The control probes were sense sequences of the target mRNA which was able to detect the double stranded plasmids (Figure 4 A). Untransfected cells identified by the DAPI nuclear staining (blue) showed no FISH signal.

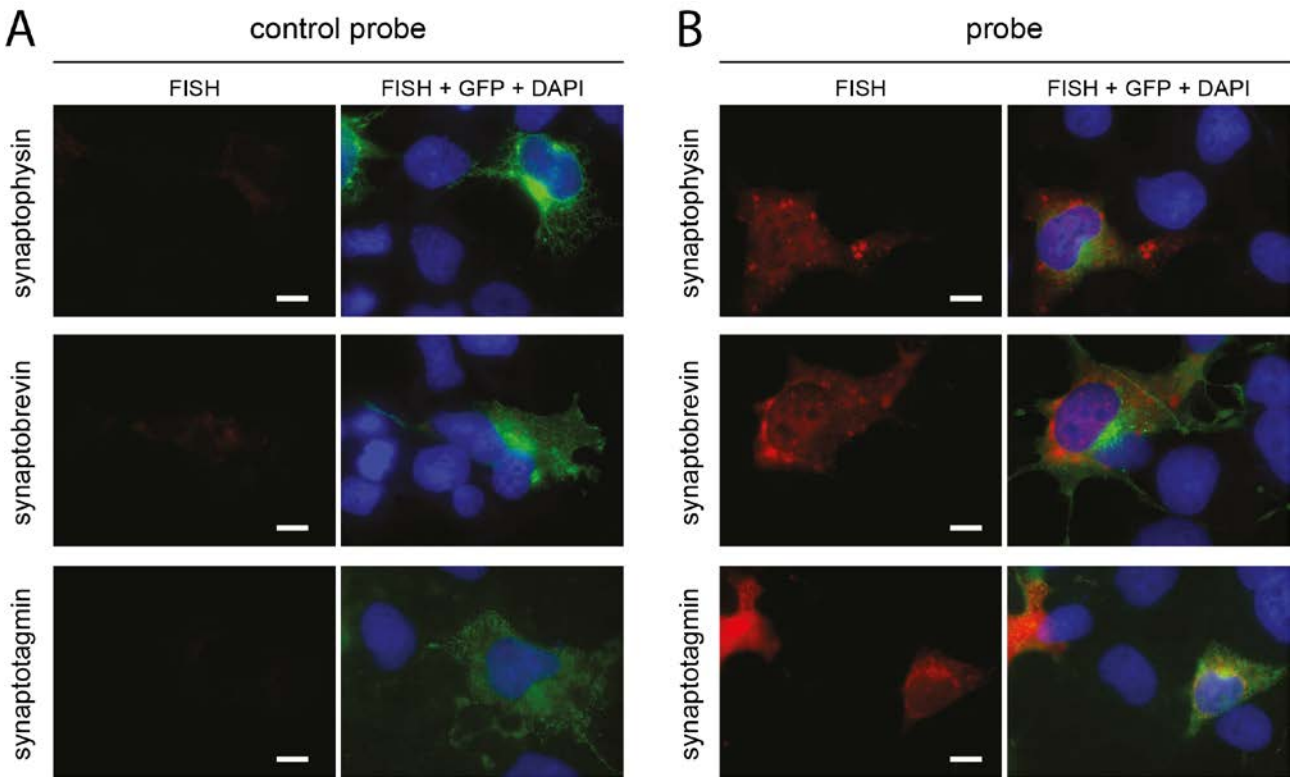

(4) Figure | Cos-7 cells transiently transfected with fusion versions of synaptic proteins. Transfected cells can be easily identified by the GFP signal (green), while untransfected cells are revealed by DAPI staining (blue). (A) Only little signal can be observed within transfected cells when using the control probes (red). The signal originates from specific annealing of the probes to the plasmids that contain both sense and anti-sense sequences of the respective genes. (B) Only transfected cells contain high FISH signal (red). These epifluorescence images were scaled identically for each channel. Scale bars, 10 µm.

As the other control, I performed FISH to detect the transcripts but this time using a different set of probes against the UTRs of the mRNAs of the three synaptic proteins and compared the staining results of the two sets of probes. The spot densities of both sets were not statistically different from each other (Figure 5) implicating that the staining was indeed specific and reliable.

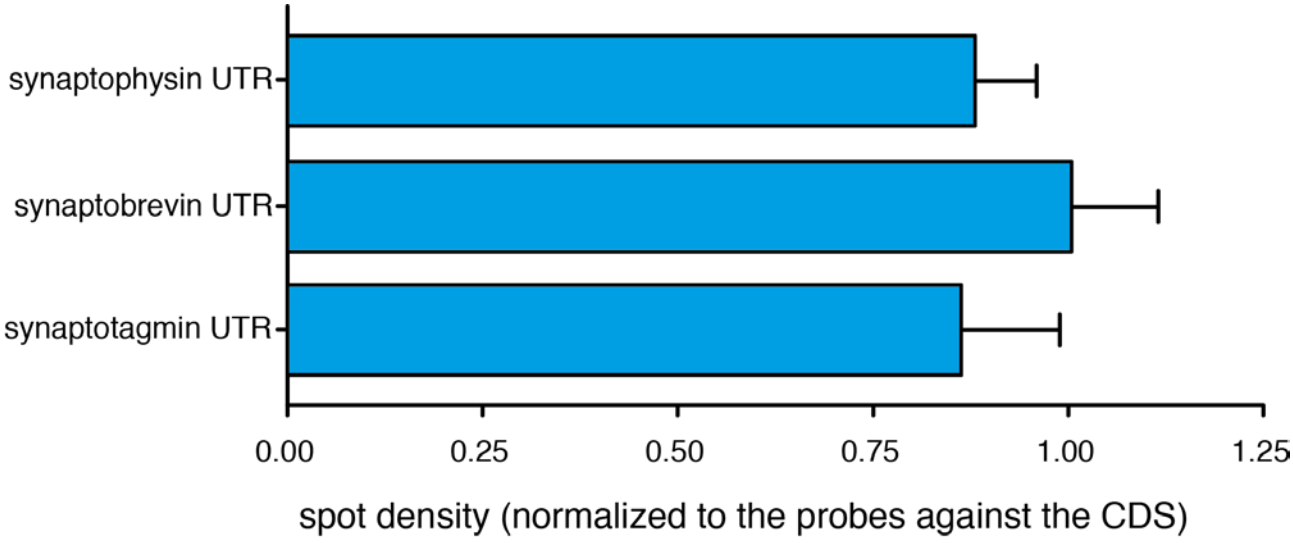

(5) Figure | Comparison of spot densities between probes targeting the UTRs and CDSs. No statistically significant difference could be seen for any of the mRNAs of the three synaptic proteins (n = 5 to 6), suggesting that a representative population was detected.

2.1.2. Three probes per RNA target are sufficient for reliable detection

True signal can be discriminated from unspecific binding by fluorescence intensity (Figure 4). Using only one probe was not sufficient to differentiate signal (grey) from background (black). This especially applies for RNAs expressed at low levels, where background might mask the true signal. In contrast, performing FISH with three different probes per RNA target increased the fluorescence intensity per spot significantly allowing reliable identification of the mRNAs (cyan).

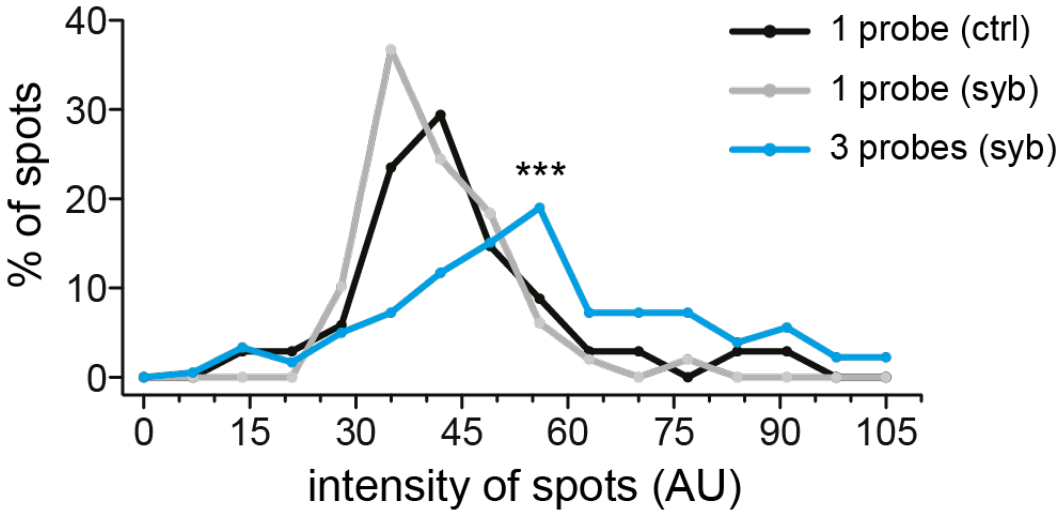

(6) Figure | Histogram of spot intensities with regard to number of probes used. Using only one probe (grey) was not sufficient to reliably distinguish from controls (black). If three probes were used (cyan), the intensity of the majority of the spots was significantly higher than the controls ($p<0.001$; t-test).

Since the protocol should be universal for all RNAs (except for very short ones like miRNAs), I decided to use only three probes per RNA. The probes must not overlap to compete for binding sites, nor have cross-reactivity with each other or other transcripts of the sample. This may already be difficult, especially for short RNAs. In the case of synaptobrevin, the three chosen probes were the only possible ones. All probes should be of the same physical properties, so that the hybridization conditions are similar for all probes, i.e length and melting temperature (T_m). If mature mRNAs are of interest, the selection criteria are even more strict as the probes should span over adjacent exons.

2.1.3. STED-FISH provides information about RNA organization

I then stained endogenous levels of mRNA of the three synaptic proteins synaptophysin, synaptobrevin, and synaptotagmin in primary hippocampal neurons. Figure 7 shows a neuron identified by synaptophysin immunostaining (cyan). Most of the FISH signal (red) was localized in the cytoplasm of the neuron. Comparison of the confocal and STED images reveal that some of the diffraction limited spots actually consist of multiple spots (cyan circles). This indicates higher numbers of mRNA molecules than apparent in confocal images, making STED more accurate.

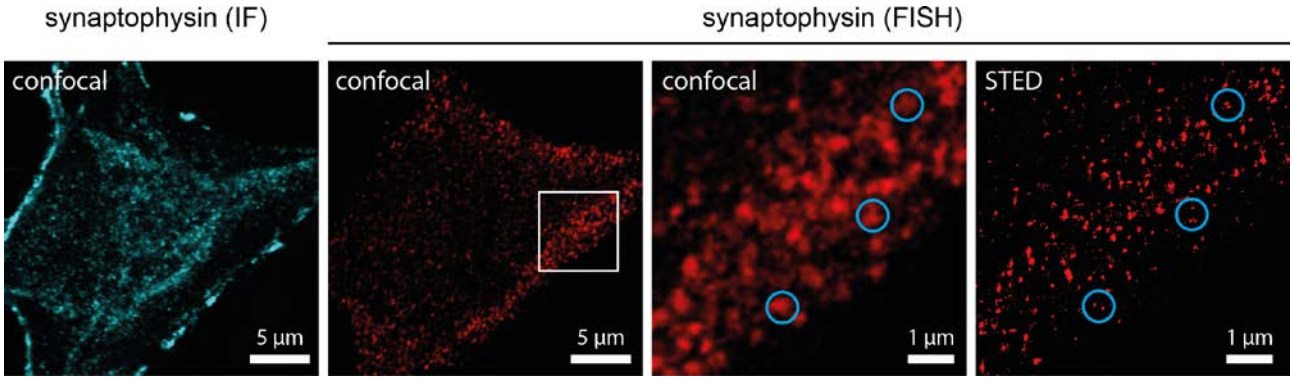

(7) Figure | STED provides more accurate information than confocal microscopy. Confocal and STED images of a neuron stained by immunofluorescence (cyan) and FISH (red) against synaptophysin protein and mRNA. Looking at the zoom-ins (white square), some of the diffraction limited spots in the confocal image consist of multiple spots revealed by STED (cyan circles). Scale bars, 5 µm (for overview of neuron) or 1 µm (for zoom-ins).

The increased resolution with STED-FISH did not only allow a more precise estimation of the mRNA numbers but also provided information about the intermolecular organization. The spots of the three synaptic proteins were approximately ~50-60 nm in size, i.e. at the resolution limit of the STED microscope used for this work (Figure 8, first three panels). In contrast, the spots of β-actin mRNA were noticeably larger and brighter (~80 nm, right panel), suggesting an organization in structures containing multiple mRNA molecules.

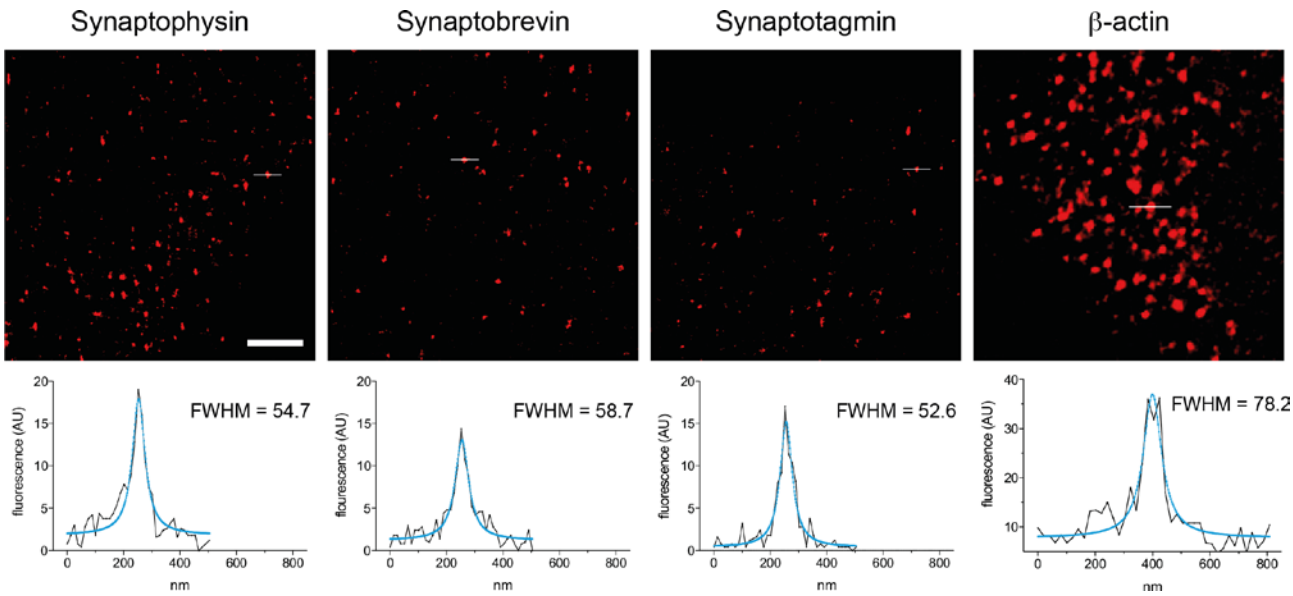

(8) Figure | STED-FISH is able to resolve mRNA organization. STED images of neurons stained by FISH against the mRNAs of synaptophysin, synaptobrevin, synaptotagmin, and β-actin (upper panel) and the respective line scans (white lines in the images, graphs in the lower panel). While the spot sizes of the three synaptic proteins was close to the resolution limit of our microscope (~50-60 nm; first three columns), β-actin showed larger spots (~80 nm; fourth column). Also note the scaling of the y-axis, showing approximately double the fluorescence intensity for β-actin. Scale bar, 1 µm.

2.1.4. STED-FISH is able to monitor mRNA levels qualitatively

FISH can monitor RNA levels qualitatively based on the spot number in relation to the volume of the cell. This type of quantification may not be as accurate as biochemical assays like quantitative PCR (qPCR). Those methods, however, usually require more material (i.e. cells). mRNA levels of the three synaptic proteins and of the general housekeeping protein β-actin were investigated with regard to neuronal development *in vitro*. The mRNAs, as measured by spot density, of all four proteins increased with maturation (Figure 9; cyan, red, green, and yellow), while the spot density of the control probes remained at the baseline (black). Interestingly, synaptophysin showed the largest relative change until day *in vitro* (DIV) 21 and reduced the expression thereafter.

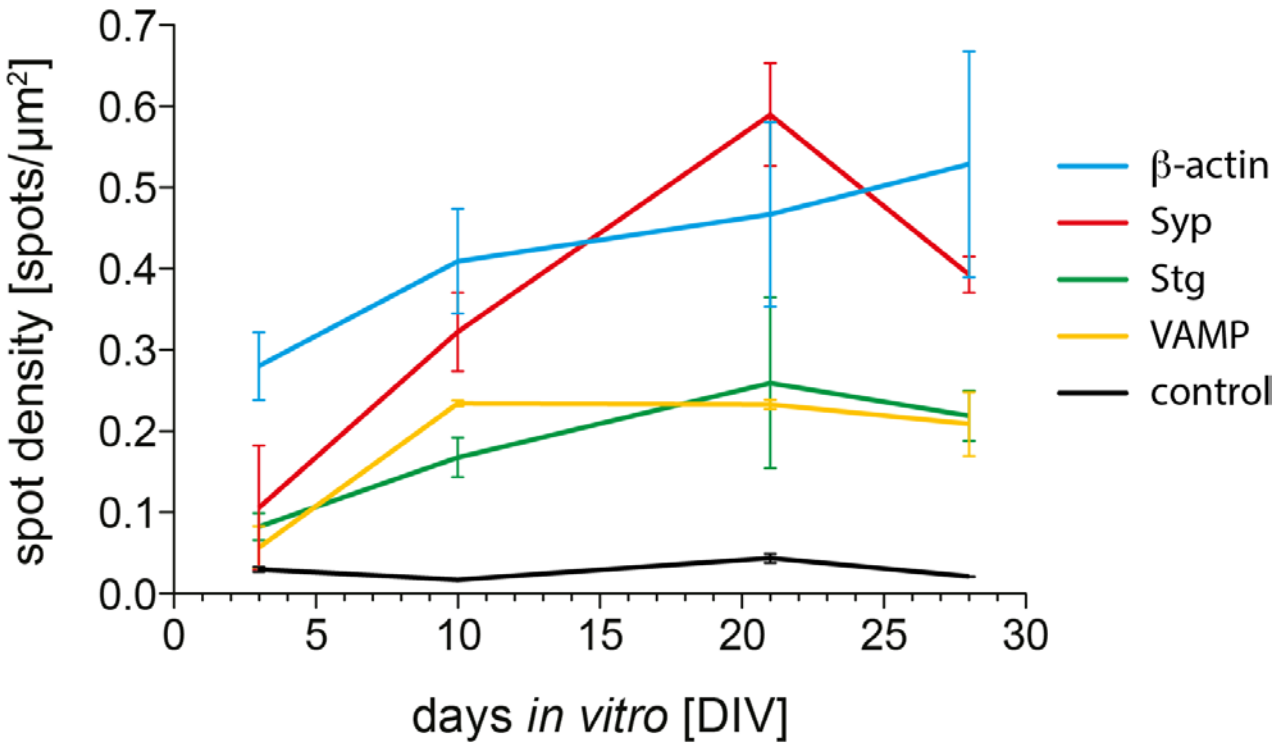

(9) Figure | Changes in mRNA levels with respect to age in vitro. The numbers of mRNA molecules for β-actin and the three synaptic proteins increase with age while the control stayed on the baseline level. Interestingly, the spot density of Syp FISH (red) increased 5-fold until DIV 20 and decreased to the 4-fold of the initial level at DIV 28.

2.2. Establishing a microscopy-based diagnosis method for AD

Despite Alzheimer's disease (AD) being the most common form of dementia, its diagnosis mainly relies on cognitive tests. This means that the patients already show symptoms of cognitive impairment at the time of diagnosis, due to potential neuronal damage possibly caused by abnormal Aβ and/or tau assemblies (Andreasen and Blennow, 2005). Therefore, I turned to STED microscopy analyzing Aβ and tau assembly numbers and sizes in human CSF to develop a novel diagnosis method. Compared to only analyzing their concentrations in CSF or the cognitive states of the patients, my approach might 1) diagnose the disease more reliably and with higher accuracy. STED is able to additionally provide information about particle size and organization, which is thought to be a major factor of the neuronal toxicity (oligomers vs insoluble fibrils, also see Section 1.4); 2) detect the disease at prodromal stages when toxic Aβ and tau species have formed but have not affected the patients cognition; and 3) monitor disease severity and thus disease progression.

To characterize Aβ and tau assemblies, I analyzed human CSF samples of 36 AD patients, 21 controls, and 11 mild cognitive impaired (MCIs). The underlying idea was to immobilize CSF on

coverslips, immunostain for Aβ and tau, and to analyze their assembly characteristics by STED imaging (Figure 10).

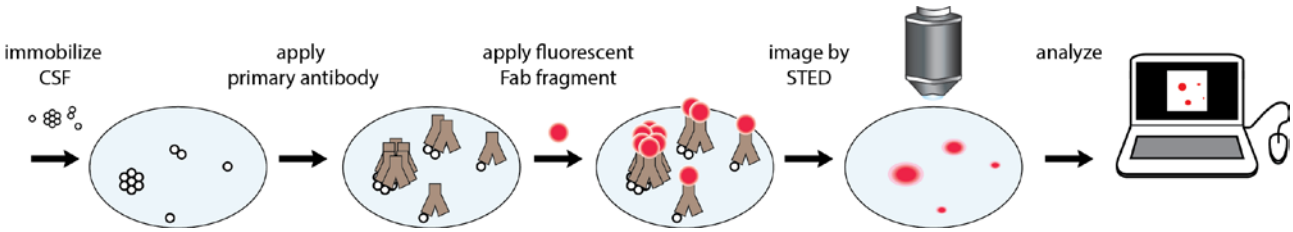

(10) Figure | Schematic overview of the experimental procedure. PLL coated coverslips were incubated with CSF. The samples were then fixed and immunostained using primary antibodies and secondary Fab fragments conjugated to Atto647N. The images obtained by STED imaging were analyzed by a custom-written MatLab macro.

2.2.1. Optimization of coverslip coating and fixation

The first challenge was to immobilize the proteins present in the CSF on coverslips for immunostaining. This procedure needs to fulfill several criteria: 1) The proteins need to be immobilized on the coverslip to endure the immunostaining procedure. 2) The procedure should represent the CSF in protein composition and organization. Especially in the case for Aβ, it is known that even at room temperature aggregates may form (Zimmermann et al., 2011). Therefore, the fixation should be as short as possible to avoid artifacts. 3) It should not interfere with the antibody recognition. Some fixatives like glutaraldehyde are known to change the epitopes so that antibodies cannot bind to their targets (Shtengel et al., 2014). I tested four coating agents and four fixation solutions for the best immunostaining result. The combination of PLL coating and 4% PFA fixation (Figure 11, cyan square) achieved the most signal, implying that most material was fixed to PLL by 4% PFA only and that the fixation procedure did not interfere with the antibody recognition. It was therefore used for all subsequent experiments.

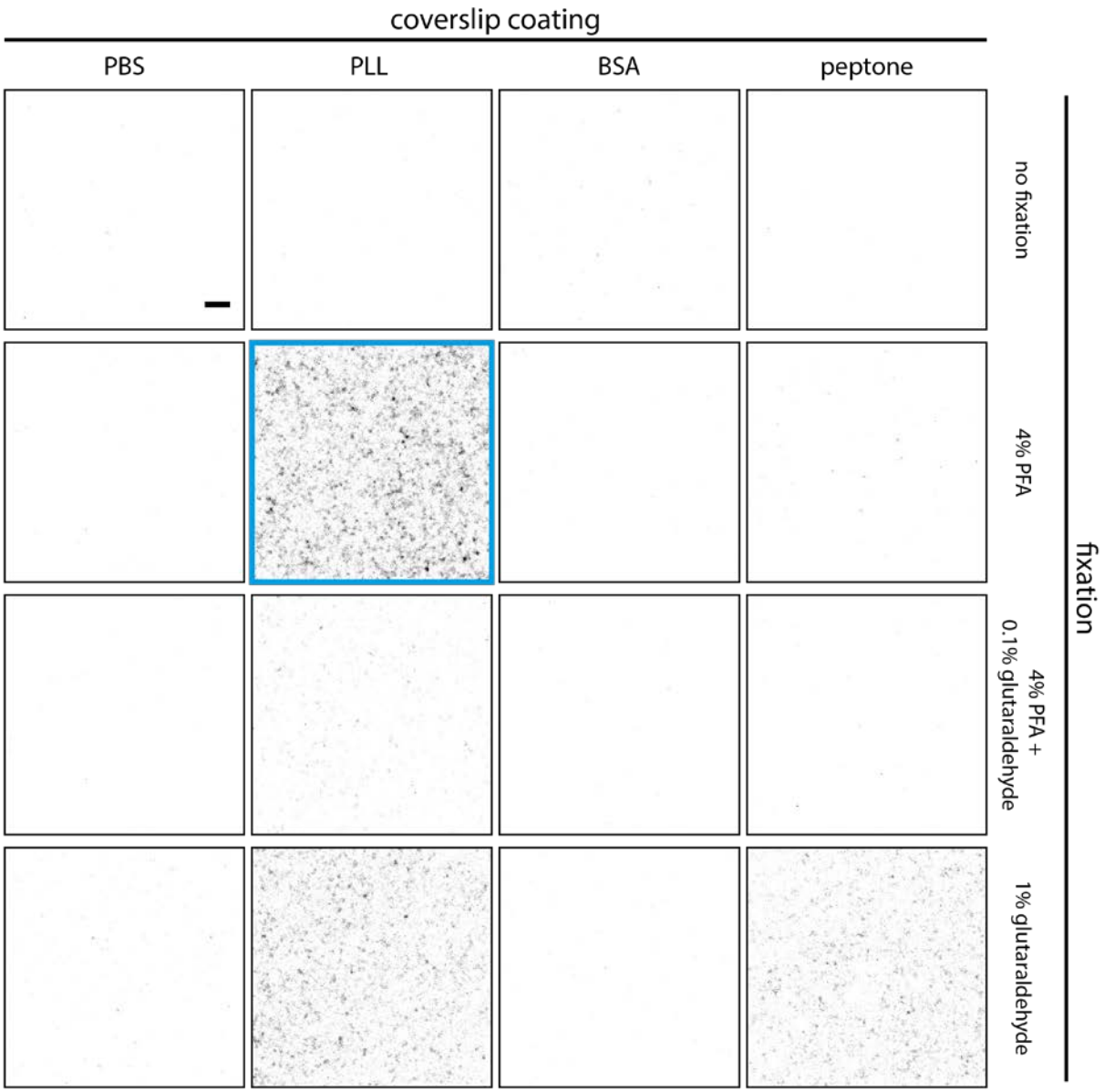

(11) Figure | Epifluorescence images of coating and fixation optimization. I tested four conditions each for coating (PBS, PLL, BSA, or peptone) for a suitable substrate and for fixation (no fixative, PFA, PFA and glutaraldehyde, or glutaraldehyde) to immobilize the CSF onto the coverslips. The combination of PLL coating and fixation with 4% PFA yielded the most immunofluorescence (cyan square). Colors inverted for better visibility. Scale bar, 2 µm.

2.2.2. Antibody selection and blocking

As for all immunostainings, the staining conditions need to be optimized for each antibody and sample type. Different antibodies bind to different epitopes with different affinities, which in turn affects the level of blocking needed to avoid poor signal-to-noise ratio or even artifacts. This is especially critical for immunostaining CSF since there are no structures for orientation as for cells or tissue samples. I tested nine different antibodies against different Aβ species, since the toxic Aβ isoform is still under debate; four against different tau versions, some of them against phosphorylated forms, since neurofibrillary tangles have been found to contain hyperphosphorylated tau proteins; as well as two oligomer-specific antibodies to detect only the potentially toxic species (see Section 4.4 for complete antibody list).

Blocking solutions for antibody stainings typically contain proteins that do not interfere with the antibody recognition to compete with the antibodies for any unspecific binding. Different blocking solutions with different blocking agents at varying amounts of protein were tested for each antibody. To test the background, only coverslips incubated with BSA instead of CSF were used (negative control), since it should be free of epitopes and therefore show only little signal. Figure 12 shows the blocking optimization for a selection of four antibodies. The 6E10 and the pan tau antibody are thought to detect all forms of Aβ and tau, respectively, while ab10148 and ab12267 were reported to only recognize specific Aβ species (see Section 4.4 for details).

Similarly to numerous other previous studies on Aβ in human CSF (e.g. Pirttilä et al., 1994, Maddalena et al., 2004), 6E10 was selected for the investigation due to its high sensitivity. Its property to potentially detect all Aβ species might allow the acquisition of a more complete protein profile of the CSF. Similarly, I chose the pan tau antibody for investigation of the tau CSF contents. Other antibodies were not used for further experiments due to poor staining results.

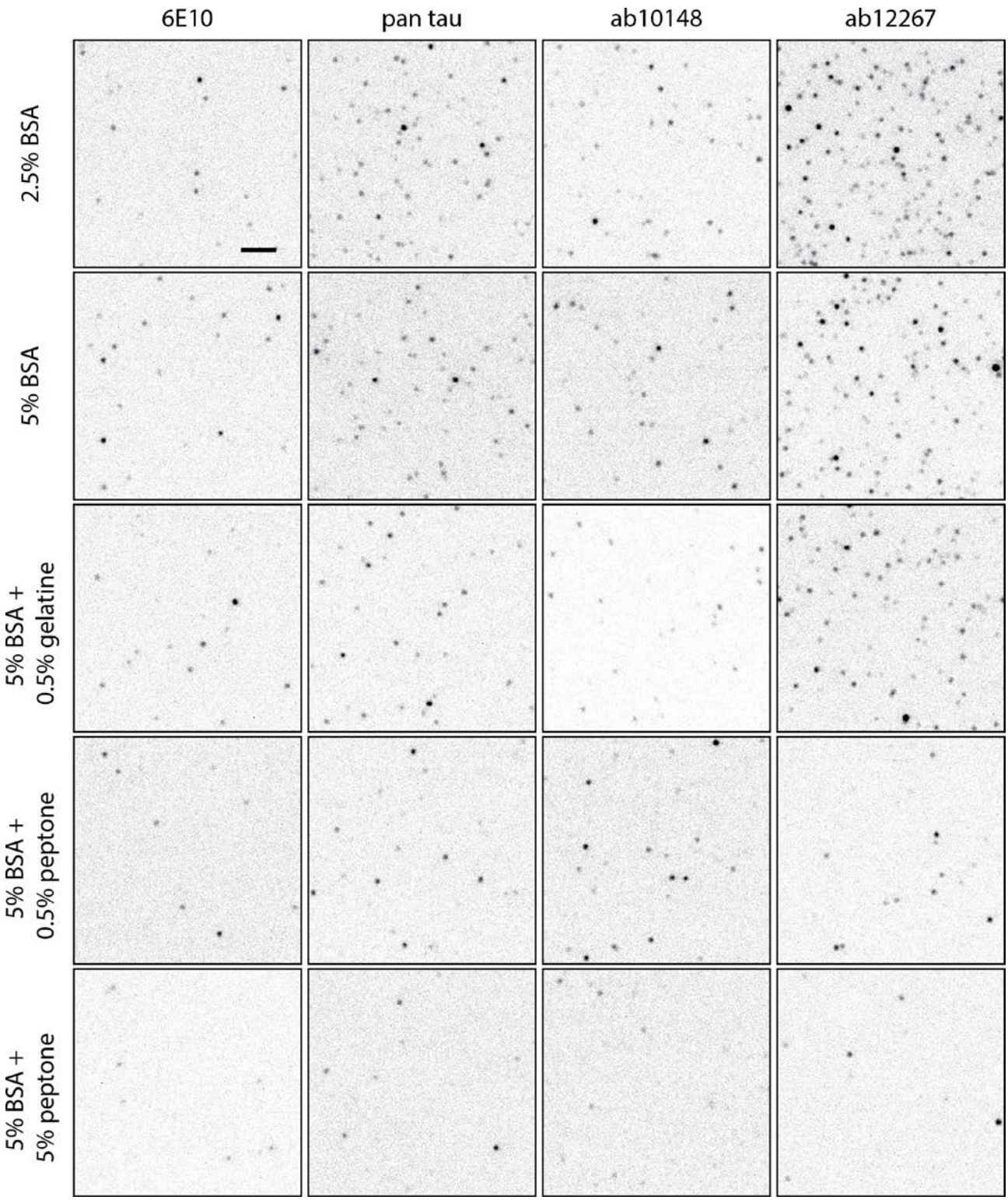

(12) Figure | Epifluorescence images of the optimization of blocking conditions. Coverslips were incubated with BSA only instead of CSF (negative control) and immunostained as described in Methods using different blocking solutions. Using the strongest blocking (5% BSA plus 5% peptone) obtained the fewest unspecific staining and was therefore used for all experiments. All images were scaled identically. Images were inverted in color to provide better visual representation. Scale bar, 2.5 µm.

2.2.3. Super-resolution is able to separate assemblies of different sizes

Confocal images of CSF immunostained against Aβ showed many spots with many of them touching or overlapping each other. Imaging the same samples with STED provides more accurate information due to the increased resolution. Similar to STED-FISH (Figure 7), some diffraction limited spots in the confocal images actually consisted of multiple individual spots which offered more precise numbers of Aβ assemblies (Figure 13 A, red circles). In addition, a line scan over the same representative spot imaged in confocal and STED mode (cyan circle) showed the resolution limits of both techniques (~277 nm for confocal and ~45 nm for STED, Figure 13 B). The higher resolution of STED may help to identify the size of the toxic species.

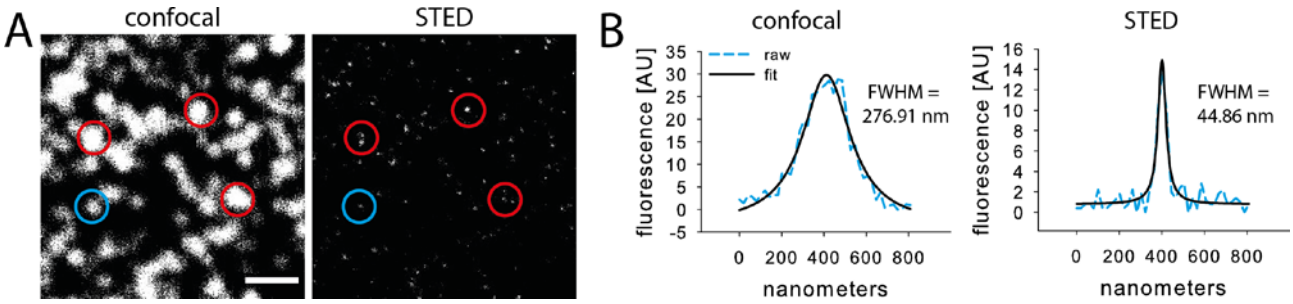

(13) Figure | Comparison of immunostained CSF imaged by confocal and STED microscopy. (A) CSF was immunostained as described in Methods and imaged in confocal (left) and STED (right) mode. The increased resolution of STED offers more details about the composition of Aβ assemblies in the CSF. With confocal, all three spots highlighted by the red circles can only be identified as one spot. In contrast, STED is able to resolve them originating from multiple or one single, bright object. (B) Raw (cyan) and fitted (black) line scans of the same individual spot (cyan circles in panel A). Confocal microscopy is limited by diffraction and thus is only able to resolve object to ~ 250 nm (full width of half maximum, FWHM) while STED can differentiate spots which are ~ 25 times smaller (FWHM of ~ 50 nm in both x- and y-dimension). Scale bar, 1 µm.

Next, to test whether STED is indeed capable of discriminating assemblies of different sizes, I immunostained low- (LMW) and high-molecular weight (HMW) assemblies of in vitro synthesized Aβ peptides. LMW Aβ showed small spots of similar sizes, while HMW Aβ showed spots of different sizes with many remarkably larger than for LMW Aβ (Figure 14 A). Analysis of the STED images showed a clear difference between the two samples (Figure 14 B). LMW Aβ spots were smaller and dimmer (indicating fewer Aβ molecules per spot) than HMW Aβ spots. Assembly sizes were determined by size exclusion column (for details, see Section 4.8.1.).

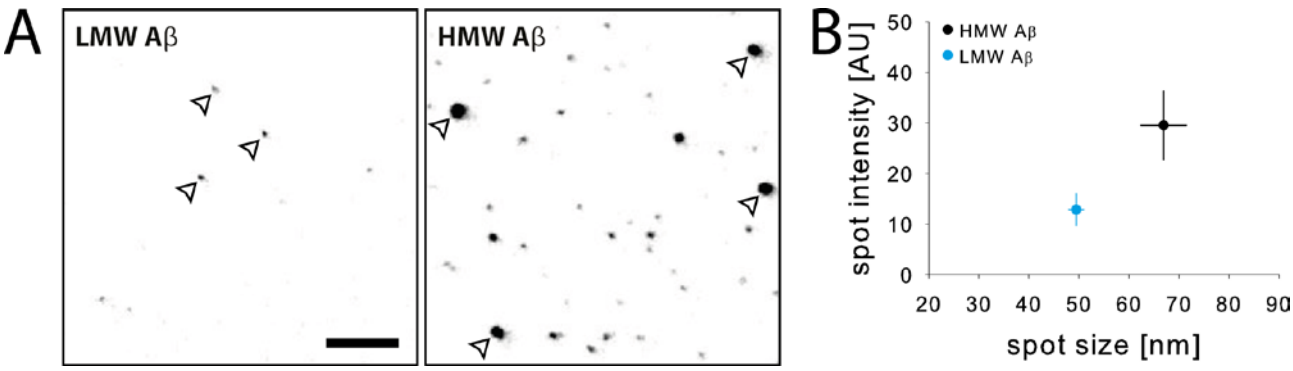

(14) Figure | STED assessment of low (LMW) and high molecular weight (HMW) Aβ assemblies produced in vitro. (A) Representative STED images of synthetically produced LMW (left) and HMW Aβ assemblies (right). Colors were inverted for better visibility. Scale bar, 1 µm. (B) The quantification shows that the two Aβ species can be discriminated from each other by either spot size or intensity. Note that the mean spot size of the LMW assemblies is close to the resolution limit of the microscope. Graph shows means ± SEM.

These results show that I successfully established an immunostaining protocol for Aβ and tau of human CSF for STED microscopy capable of discriminating assemblies of different sizes.

2.2.4. AD patients show fewer, smaller, and dimmer spots than controls

CSF samples from 36 AD patients, 21 controls, and 11 MCI were immunostained for Aβ and tau, imaged by STED, and analyzed as described in Methods. Figure 15 A shows representative STED images of CSF samples from controls (upper panel) and AD patients (lower panel) immunostained for Aβ. Intriguingly, AD patients showed fewer, smaller, and dimmer spots (Figure 15 B). This may be accounted by sequestration of Aβ peptides into amyloid plaques in the brain, thereby reducing the amount of CSF Aβ.

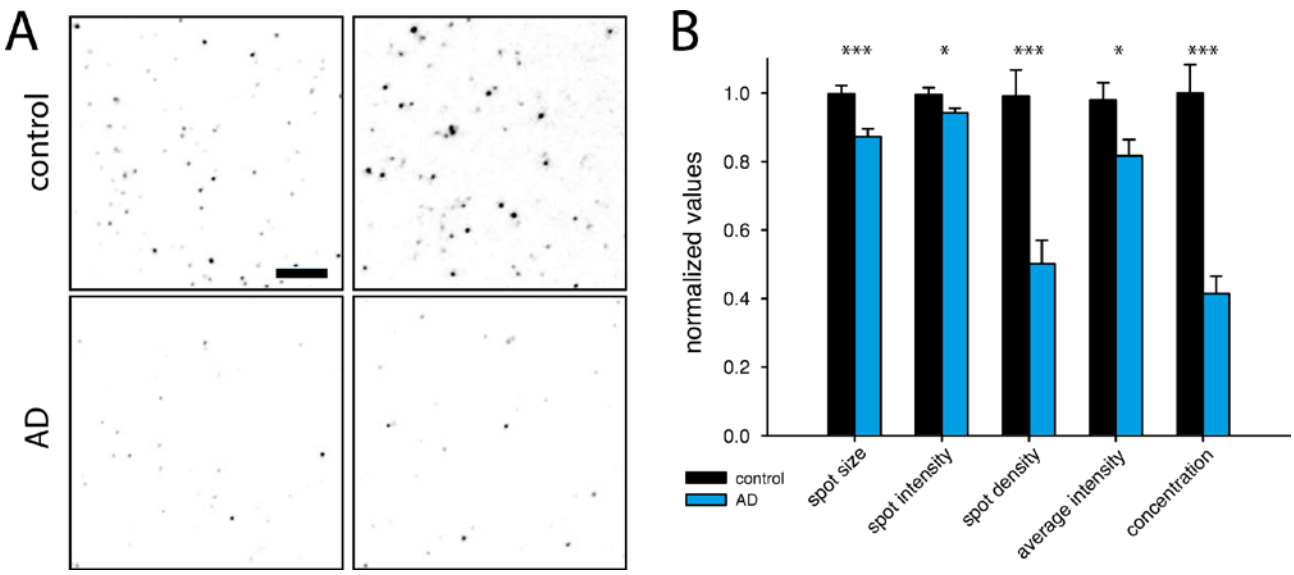

(15) Figure | Analysis of CSF Aβ by STED imaging. (A) Example STED images of CSF immunostained for Aβ. AD patients (lower panel) show smaller and fewer spots than controls (upper panel). Images were color inverted for better visibility. Scale bar, 1 µm. (B) Bar graph of the mean values of the four STED parameters (spot size, spot intensity, spot density, and average intensity) and Aβ concentration determined by ELISA. Controls show statistically significant higher values than AD patients for each parameter (* < 0.05; *** < 0.001).

2.2.5. STED parameters of tau increased prediction accuracy

With the means of all four parameters (spot size, spot intensity, spot density and overall intensity) being significantly different in AD patients and controls (Figure 15 B), I analyzed CSF samples with regard to tau (Figure 16). Despite none of the STED parameters being significantly different between AD patients and controls (Figure 16 B), combination of Aβ and tau data increased prediction accuracy from approximately 76% for both sensitivity and specificity to 79% and 87%, respectively (Figure 16 C-E), with sensitivity defined as the percentage of AD patients that were correctly identified and specificity defined as the percentage of controls that were correctly identified. The underlying discriminator functions F(Aβ) and F(Aβ, tau) were obtained by combining all four parameters in a linear equation (Equation III and IV). Finally, the STED values F(Aβ) and F(Aβ, tau) correlate well with ELISA measurements of Aβ (Figure 17).

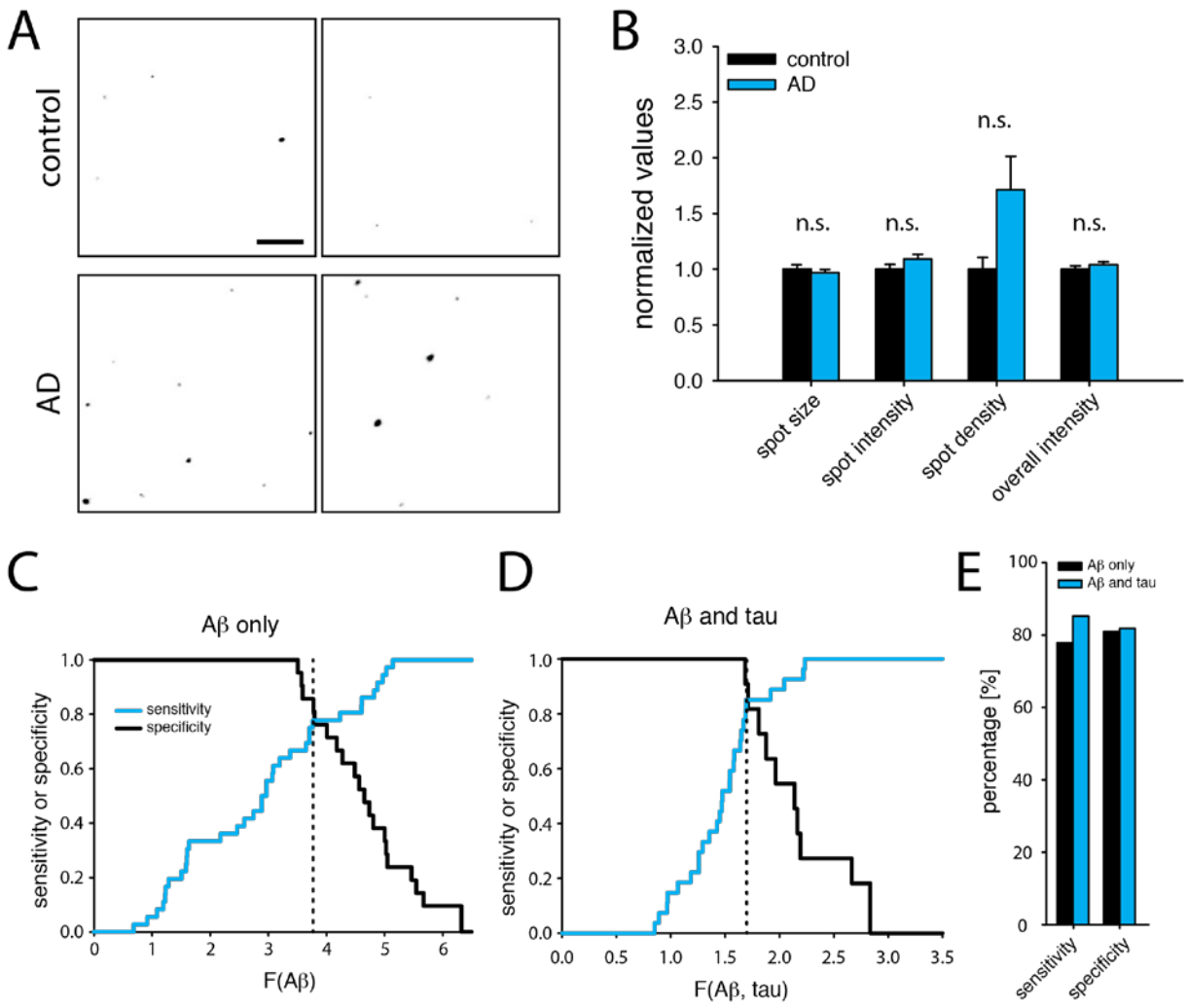

(16) Figure | Analysis of CSF tau by STED imaging and prediction accuracy of STED. (A) Representative STED images of CSF immunostained for tau. AD patients tend to show more spots. Images were color inverted for better visibility. Scale bar, 1 µm. (B) Bar graph of the mean values of the four STED parameters (spot size, spot intensity, spot density, and average intensity). Differences in neither of the four parameters were statistically significant (n.s.) (C) Prediction accuracy of the STED-based assay according to the cut-off for the F(Aβ) value or (D) F(Aβ, tau) value (dashed lines). (E) Improved prediction accuracy when Aβ and tau data is combined (cyan) compared to Aβ alone (black).

$$F_{A\beta} = a \cdot \frac{A\beta_{spotsize}}{A\beta_{spotintensity}} + b \cdot \frac{A\beta_{spotdensity}}{A\beta_{totalimageintensity}}$$

(III) Equation | Discriminator function using STED parameters from Aβ data. This equation assigns a value to each patient according to the STED parameters for Aβ, where a and b are constants and b surpasses a by 3-4 fold. Best separation of AD and controls was achieved with a cut-off value of ~3.7.

$$F_{A\beta,tau} = a \cdot \frac{A\beta_{spotsize}}{A\beta_{spotintensity}} + b \cdot \frac{A\beta_{spotdensity}}{tau_{spotintensity}}$$

(IV) Equation | Discriminator function using STED parameters from Aβ and tau data. This equation assigns a value to each patient according to the STED parameters for Aβ and tau, where a and b are constants and both left at 1. Best separation of AD and controls was achieved with a cut-off value of ~1.7.

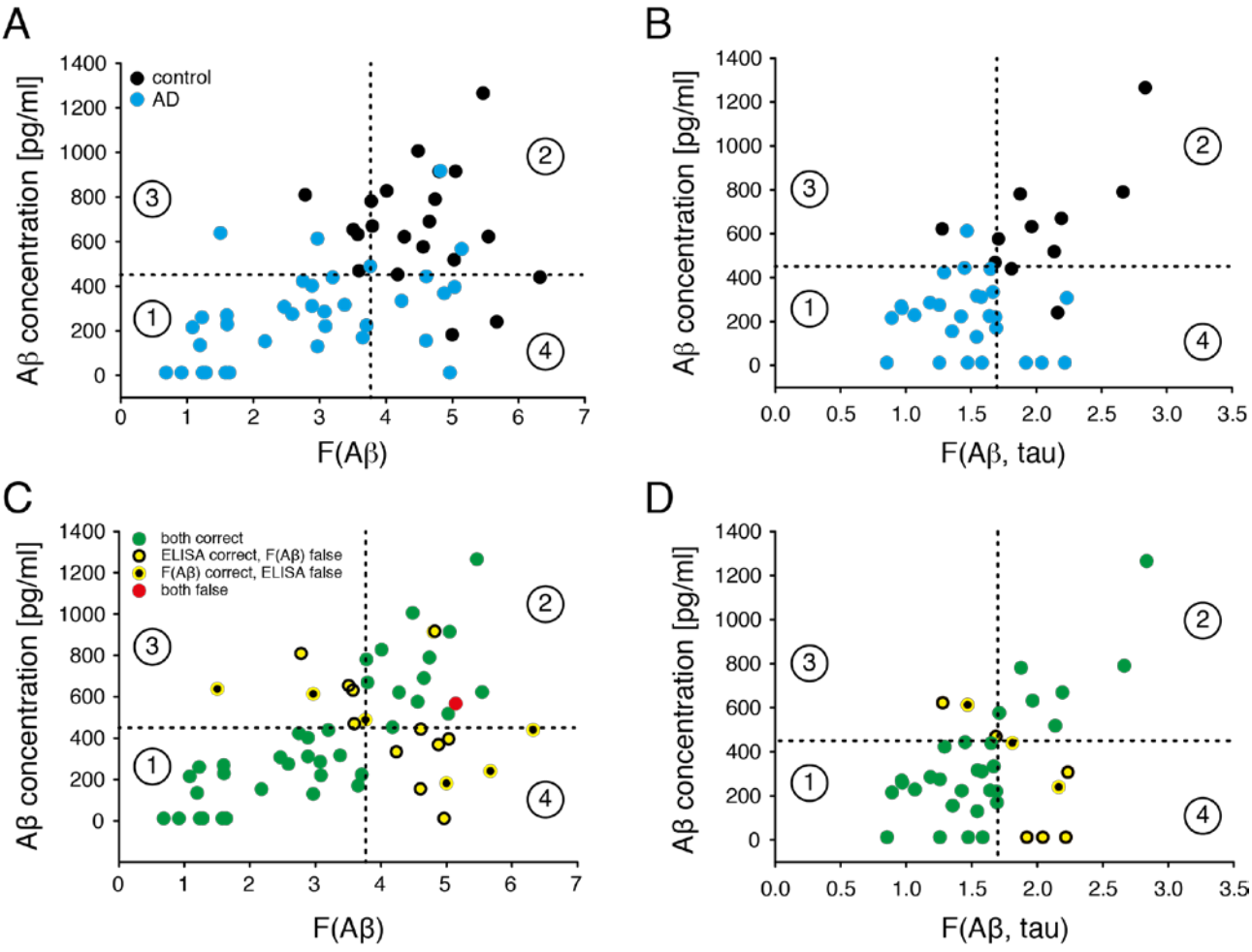

(17) Figure | Comparison of STED and ELISA prediction accuracies. (A) F(Aβ) values and (B) F(Aβ, tau) values are plotted on the X-axis against Aβ concentrations determined by ELISA on the Y-axis; controls are displayed in black, AD patients in cyan. The dotted lines indicate the cut-off values used to separate AD patients from controls at 450 pg/ml for ELISA and 3.77 for F(Aβ) or 1.70 for F(Aβ, tau), respectively. The four regions within

the graphs represent: (1) patients identified as controls by both ELISA and STED; (2) patients identified as AD by both techniques; (3) patients identified as controls by ELISA but as AD by STED; (4) patients identified as AD by ELISA but as controls by STED. It is evident that most patients fall into the areas (1) and (2) indicating identical prediction by both techniques for the majority of the patients. (C-D) For graphic view of identification accuracies, the same graphs are displayed color-coded as indicated in the legend. The green dots dominate indicating that both techniques identified most of the patients correctly.

2.2.6. STED parameters of two MCI patients were within AD range

The same method was applied to patients with mild cognitive impairment (MCI, see Section 4.8.3.). Two of the MCI patients developed full AD during the course of the study and were placed close to the AD average of the STED assay (Figure 18). This indicates that STED might have the capability to predict AD at prodromal stages.

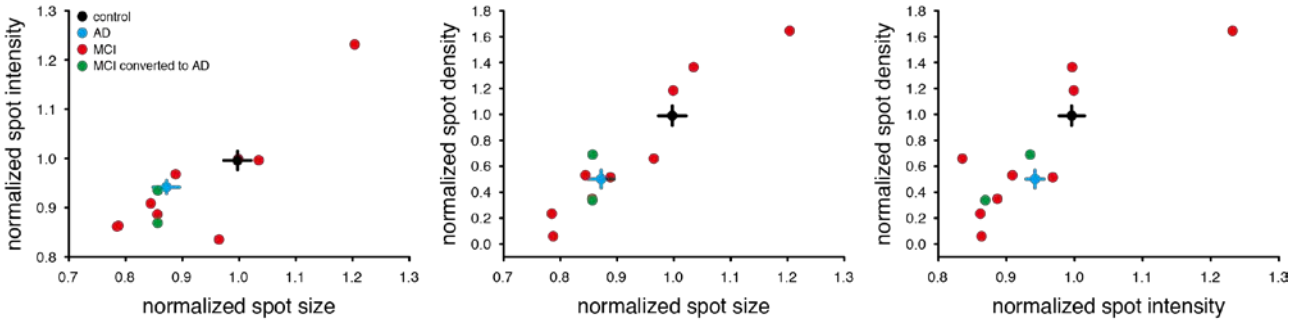

(18) Figure | STED values of MCI patients with respect to the averages of AD patients (grey) and controls (black). MCI patients are indicated by red dots, with the two MCIs that converted to full AD during the study which are depicted in green. Note that the green dots are close to the AD average (cyan).

3. Discussion

In this work, I have applied STED microscopy - as a representative for super-resolution microscopy techniques - to two applications: fluorescent *in situ* hybridization (Section 2.1) and diagnosis of Alzheimer's disease (Section 2.2). Due to the increased resolution of STED, the methodologies needed to be optimized for the needs. This works shows that using STED with well established methods provides more accurate information compared to conventional confocal microscopy. For both cases, STED was able to reveal multiple spots per individual diffraction limited spot. This allowed to characterize mRNA levels and organization of the synaptic proteins synaptophysin, synaptobrevin, and synaptotagmin and the housekeeping protein β-actin more accurately than by conventional light microscopy (Section 2.1.3.). β-actin mRNA seems to be organized in units of multiple RNA molecules as those particles were larger and brighter compared to the spots of the synaptic proteins (Figure 8).

This first application of super-resolution microscopy to medical diagnosis was able to discriminate controls from AD patients by analyzing images of immunostained CSF samples. The assay uses the parameters number and size of assemblies and number of Aβ or tau molecules per assembly, which allowed a separation with a specificity of ~87% and a sensitivity of 79% (Figure 16). This accuracy is comparable to the one achieved by ELISA, the current gold standard in the field. In addition, two of the MCIs who converted to full AD during the study showed similar Aβ profiles as AD patients (Figure 18). Despite being only a very small sample size, these side findings encourage for further investigations.

3.1. Technical limitations

Both applications posed a particular challenge compared to other targets or sample types, like organelle marker or cell culture systems. In both cases in this study, the stainings were difficult to be confirmed by structure, since the images consisted of seemingly random spots. For staining and imaging CSF, there is only a single layer of molecules to be imaged, which adds to the difficulty. Due to the low amount of material, there is only little fluorescence in the first place, thereby decreasing the signal-to-noise ratio and resolution. In addition, drifting might cause not only reduction of the signal but even loss of the initially low fluorescence.

3.2. Technical limitations of FISH

3.2.1. Loss of RNA

Another issue is the loss of RNAs during the experimental procedure. For one, contaminations with widespread present RNases may degrade a large percentage of RNAs, including the target mRNA and thereby reducing the FISH signal. Second, the fixative PFA fixes cells mainly based on cross-linking proteins. Due to repeated washings under harsh conditions (i.e. formamide and temperatures well above room temperature) non-proteinaceous molecules like RNAs may be lost and can therefore not be detected by FISH. The issue of signal loss can be exacerbated by masking of the binding sites for the probes on the mRNA molecules by translating ribosomes or other RNA-binding proteins.

3.2.2. Inefficient blocking

Many blocking solutions for *in situ* hybridization protocols include sheared Salmon sperm DNA to block unspecific binding of the probes. These random sequences compete with the probes with DNA/RNA-binding proteins, other nucleic acids, and other unspecific interactions due to the same nature. However, its blocking capabilities may be suboptimal due to its size. According to different manufacturers, the size of most DNA molecules is larger than 1000 bp, which is ~2-5x the size of *in situ* hybridization RNA probes and ~20-50x of DNA probes. The cytosol is densely filled with protein which are cross-linked by fixation. Considering that one nucleotide is generally larger than one amino acid, it seems quite plausible that many unspecific binding sites of the probes are not blocked by the Salmon sperm DNA because they cannot reach the binding sites the probes can due to their size. To alleviate this issue, I used Salmon sperm DNA that has been further processed by sonication to sizes around 200 bp by the lab of Andre Fisher, DZNE, Göttingen, Germany.

3.2.3. Signal amplification

In principle, weak signal could be amplified by increasing the number of probes per target, by increasing the number of fluorophores per probe, and/or by using indirect labeling. Increasing the number of probes per target may be difficult to achieve. Designing probes for transcripts that are short or contain sequences similar to others (e.g. different isoforms) might not be possible without

cross-reactivity. Using many probes per target sequence might increase the size of the resulting spot. Having too many fluorophores in close proximity may also result in auto-quenching of the fluorophore (Wolfbeis, 2005). Increasing the number of fluorophores per probe also increases the costs. There are two approaches for indirect labeling: use of antibodies and the use of enzymes. Using a primary-secondary or even an added tertiary antibody will amplify the signal for each tier since multiple secondaries can bind to a single primary antibody (similar for tertiary antibodies to secondaries). Using enzymes will produce signal that diffuses within the cell. Both amplification approaches result in a larger spot and thereby decreasing the resolution. A balance between sensitivity and accuracy based on resolution needs to be chosen well.

3.3. Technical limitations - AD

3.3.1. Limitations of the field

A major issue in the field is that it is difficult to compare between studies. One factor is differences of sample acquisition. The protein levels in the CSF are dependent on the circadian rhythm. Therefore changes in the time of day when the lumbar puncture is performed may affect experimental results (Cicognola et al., 2015). Other artifacts may occur due to differences in processing of the CSF, i.e. speed of processing after lumbar puncture, centrifugation duration and properties, as well as the material of the equipment and containers used. Heterogeneity in the plastic composition of the equipment are known to absorb Aβ and thereby may deplete the CSF of Aβ for further analysis (Fourier et al., 2015). Furthermore, the way the samples are stored may also affect the protein composition of the CSF. Especially, thaw-freeze cycles are known to affect tau concentrations (Schoonenboom et al., 2005).

Another issue is the study cohort. Suitable controls need to be included (age, ethnicity, etc). However, obtaining CSF from subjects with no medical condition was not possible due to the local ethics commission. This would allow monitoring the disease onset, which is essential to develop therapies. Moreover, it is hard to find a study cohort that is in general representative of the (local) population.

The current diagnosis methods still relies on medical assessments, which have inaccuracies especially when dealing with early cases of AD. Since the development of the STED-based diagnosis depends on initial medical classification of the patients, the assay may not be able to reach full accuracy. This issue is illustrated by the fact that some patients were diagnosed

differently in the course of the study, since accurate identification of similar dementia forms is difficult (Hulstaert et al., 1999). This interfered with the analysis and the development of a discriminator function. This can be countered by long-term studies. Further longitudinal follow-up studies are needed to confirm the results of this study and especially to test its prediction accuracy for AD at prodromal stages. Ideally, young adults would be followed until their death. CSF samples of those patients could be analyzed with respect to the patients' long-term medical history and autopsy data for more accurate diagnosis.

3.4. Outlook

The STED-based diagnosis method of AD and other aggregopathies might be remarkably improved by the development of new affinity probes. First, isoform- or conformation-specific affinity probes may refine the prediction accuracy by focusing on the toxic protein species only. Second, using smaller affinity probes like nanobodies or aptamers reduces the distance between the epitope and the fluorophore, therefore the spot size. This provides more precise information about the actual physical dimensions of the target, in this case Aβ and tau particles. This might allow even the identification of the toxic species. Future generations of microscopes and novel microscopy techniques with improved resolution may further increase the precision.

Another factor that is often neglected is the influence of the dye on the staining results. The opto-physical properties of the dye determine the image quality, like speed of bleaching or quantum yield. Quantum dots, for example, have a high quantum yield with low photobleaching. However, other factors need to be considered as well. Quantum dots are relatively large in size (5-50 nm; Massey et al., 2015). This would affect the diffusion properties of the affinity probe remarkably and thus impair tissue penetration, which is especially important when considering quantum dots for labeling of oligonucleotides for FISH. The size of the dye also affects the resolution of the image. The larger the dye, the larger the spot and thus the worse the resolution.

Another factor to keep in mind, is the dye's general physical property. Concerning this work, Atto647N, the dye that achieved the best results for this study, is highly hydrophobic (Zanetti-Domingues et al., 2013). This may lead to unspecific binding, especially to membranes, and thus a suboptimal signal-to-noise ratio or even misleading artifacts. In extreme cases, it may cause the affinity probe to precipitate.

Therefore, these factors should be taken into account when doing a staining since re-optimization may be required. Innovations in dye development may improve the staining and imaging results in general and due to the possibility of co-stainings/co-localizations and coincidence detection.

In conclusion, this work illustrates the need for optimization of even long established methods dependent on the imaging technique and sample type used. This allows the acquisition of detailed and therefore more accurate data. Both projects presented represent first steps in the fields of RNA and medical research encouraging follow-up or new studies and re-investigation of past questions, which were not able to be answered due to the lack of resolution of conventional fluorescence microscopy.

4. Material and methods

All experiments were performed at room temperature unless otherwise stated.

4.1. General chemicals and manufacturers

The laboratory equipment and chemicals used in this work were purchased from the companies or were provided from groups of the institutions stated in the following table. For individual cases within the rest of the document, only the short company name will be given. Please refer to this table for more information.

(A) Table | List of manufacturers and institutes.

company / institute	city, state	country
Abcam	Cambridge	UK
ATTO-TEC GmbH	Siegen	Germany
Covance Inc.	Princeton, NJ	USA
Chroma Technology Corp.	Bellow Falls, VT	USA
Dako Cytomation	Glostrup	Denmark
Eppendorf	Hamburg	Germany
Eurofins Scientific GmbH	Hamburg	Germany
GE Healthcare	Little Chalfont	UK
Gerhard Menzel GmbH	Braunschweig	Germany
Gibco	Paisley	UK
Instituto de Salud Carlos III	Madrid	Spain
Invitrogen	Carlsbad, CA	USA
Leica Microsystems GmbH	Mannheim	Germany
Life Technologies	Carlsbad, CA	USA
Lonza GmbH	Cologne	Germany
Max-Planck-Institute for Biophysical Chemistry	Göttingen	Germany
Max-Planck-Institute for Experimental Medicine	Göttingen	Germany
Merck Millipore	Darmstadt	Germany

company / institute	city, state	country
New England Biolabs	Frankfurt am Main	Germany
Newport Spectra-Physics GmbH	Darmstadt	Germany
Olympus Corporation	Tokyo	Japan
PAA Laboratories GmbH	Clöbe	Germany
Peptide Specialty Laboratory (PSL)	Heidelberg	Germany
AJ Roboscreen GmbH	Jena	Germany
Seqlab	Göttingen	Germany
Sigma Aldrich	St. Louis, MO	USA
Synaptic Systems	Göttingen	Germany
The Mathworks Inc.	Natick, MA	USA
Universitätsklinkum Tübingen	Tübingen	Germany
University Medical Center	Göttingen	Germany

4.2. Buffers and solutions

Phosphate-buffered saline (PBS): 137 mM NaCl, 2.7 mM KCl, 10 mM Na_2HPO_4, 2 mM KH_2PO_4; pH 7.4.

High salt PBS: 500 mM NaCl, 2.7 mM KCl, 10 mM Na2PO4, 2.0 mM KH2PO4; pH 7.4

Paraformaldehyde (PFA): 4% PFA (Merck) in PBS. *Preparation:* 8 g PFA was dissolved in 180 ml de-ionized water by mixing at mild heating and addition of 200 µl 10 M NaOH. After adding 20 ml 10x PBS, pH 7.4, the pH was adjusted to 7.4 with HCl. The solution was aliquoted and stored at -20ºC until the day of the experiment.

Tris buffer: 1 M tris, adjust to pH 8.0 with HCl.

Mowiol: 2.4 g Mowiol 4-88 (Merck), 6 g glycerol, 6 ml de-ionized water and 12 ml 0.2 M Tris buffer. *Preparation:* The chemicals were mixed up to 5 days at mild heating and adjusted to pH 8.5 with HCl. The solution was aliquoted, flash-frozen, and stored at -20ºC.

4.3. Antibodies

(B) Table | List of antibodies.

target	company/ institute	catalogue number / clone	host
Aβ	Synaptic Systems	218511 9D5H6	mouse monoclonal
Aβ	covance	SIG-39300 (6E10)	mouse monoclonal
Aβ	Bayer lab	167	mouse
Aβ	Synaptic Systems	218211 NT244	mouse monoclonal
Aβ	Synaptic Systems	218111 NT78	mouse monoclonal
Aβ	Synaptic Systems	218311 157	mouse monoclonal
Aβ	Synaptic Systems	218011 248	mouse monoclonal
Aβ	Abcam	ab10148	rabbit polyclonal
Aβ	Abcam	ab12267	rabbit polyclonal
APP	Synaptic Systems	127002	rabbit
tau	Dako Cytomation	A0024	rabbit
p-tau	Abcam	ab4856	rabbit
p-tau	Life Technologies	MN1060 AT100	mouse
p-tau	Life Technologies	MN1020 AT8	mouse
α -synuclein	Invitrogen	32-8100	mouse
α -synuclein	Abcam	ab27766	mouse
α -synuclein	roboscreen	102004001 5G4	mouse monoclonal
α -synuclein	roboscreen	102001801 10C3	mouse monoclonal
α -synuclein	roboscreen	102004701 10D2	mouse monoclonal
α /β-synuclein	Synaptic Systems	128002	rabbit
synaptophysin	Synaptic Systems	101004	guinea pig polyclonal

target	company/ institute	catalogue number / clone	host
MAP2	Abcam	ab11267	mouse monoclonal
A11	Invitrogen	AHB0052	rabbit polyclonal
OC	Merck	AB2286	rabbit polyclonal

4.4. Coverslip preparation

Thin coverslips (<100 µm, Gerhard Menzel) used for all experiments were acid-cleaned (1 M HCl overnight, then 1 M NaOH for 45 minutes). The coverslips were extensively washed with deionized water after each acid or base incubation. The coverslips were stored in 100% EtOH until flaming prior to overnight coating with poly-L-lysine (PLL; 0.1 mg/ml).

4.5. Cell culture

4.6.1. PC12 cells

PC12 cells - derived from pheochromocytoma of the rat adrenal medulla (Heumann et al., 1983) - were cultured in standard Dulbecco's modified Eagle's medium (DMEM, Lonza) enriched with 10% horse serum (Merck), 5% fetal calf serum (PAA), 4 mM L-glutamine (Sigma-Aldrich), and 100 U/ml each of penicillin and streptomycin (Lonza) at 37ºC, 5% CO_2, 90% humidity. Cells were seeded on PLL-coated coverslips of 18 mm diameter 24 hours prior to the experiment. For passaging, the cells were harvested by trypsin/EDTA (Lonza) treatment.

4.6.2. COS-7 cells

COS-7 cells - green monkey kidney fibroblast-like cells transformed by the simian virus 40 (SV40, Invitrogen) - were cultured in standard DMEM enriched with 10% fetal calf serum, 2 mM L-glutamine, and 100 U/ml each of penicillin and streptomycin at 37ºC, 5% CO_2, 90% humidity.

Cells were seeded on PLL-coated coverslips of 18 mm diameter 24 hours prior to the experiment. For passaging, the cells were harvested by trypsin/EDTA treatment.

4.6.3. Neuronal culture

Primary hippocampal neurons of newborn rats were seeded on a previously grown astrocyte layer on PLL-coated coverslips of 18 mm diameter. The neurons were cultured in Neurobasal A (Invitrogen) enriched with 2% B27 (Invitrogen), 1% glutamax-I (Invitrogen), 60 U/ml penicillin, and 20 U/ml streptomycin at 37ºC, 5% CO_2, 90% humidity.

4.6. Fluorescence *in situ* hybridization (FISH)

4.6.1. Probe design

All DNA oligonucleotides were purchased from Eurofins. The probes were designed to have similar hybridization properties using a custom MatLab (The Mathworks Inc) macro to find all non-overlapping sequences of 55 nucleotides with a GC content between 45.5% and 56.4%. Those candidates were checked for possible cross-reactions by aligning their sequences against the rat mRNA database (RefSeq, NCBI database). All candidates with more than 25% of their sequence reverse complementary to unspecific targets were removed. Sequences spanning contiguous exons were preferred to detect mature mRNAs specifically. The probes were labeled with one Atto647N fluorophore at each end. This increased the signal while avoiding self-quenching of the fluorophore and alteration of the hybridization properties. Three probes were chosen for each target resulting in, in theory, three probes with six fluorophores per target mRNA molecule. A list of the probes used can be viewed in the subsequent table (Table A).

(C) Table | List of FISH probes with their sequences and fluorophores.

target mRNA (probe name)	probe sequence (all sequences from 5’ to 3’)
β-actin (coding sequence; act#1)	TTC TCC ATA TCG TCC CAG TTG GTT ACA ATG CCG TGT TCA ATG GGG TAC TTC AGG G
β-actin (coding sequence; act#2)	AGG TCT CAA ACA TGA TCT GGG TCA TCT TTT CAC GGT TGG CCT TAG GGT TCA GAG G
β-actin (coding sequence; act#3)	ACC AGA CAG CAC TGT GTT GGC ATA GAG GTC TTT ACG GAT GTC AAC GTC ACA CTT C

target mRNA (probe name)	probe sequence (all sequences from 5’ to 3’)
synaptophysin (coding sequence; syp#1)	TTG AAC ACG AAC CAT AAG TTG CCA ACC CAG AGC ACC AGG TTC AGG AAG CCA AAC A
synaptophysin (coding sequence; syp#2)	GTG TAG CTG CCA CAC GTA GCA AAG GCG AAG ATG GCA AAG ACC CAC TGC AGC ACC T
synaptophysin (coding sequence; syp#3)	GCA TCT CCT TGA TAA TGT TCT CTG GGT CCG TGG CCA TCT TCA CAT CGG ACA GGC C
synaptophysin (UTR; syp_utr#1)	AAC AGC AAA GAC AGT TAG GGT CTC CTG GGT TGA GGG GTG GAG ACC TAG GAT ATG G
synaptophysin (UTR; syp_utr#2)	TCC TCT CTC TAC AGA GGT TAT CTC CTC TCT GCC CGT TTC ACC CAA GCC TCC TCC A
synaptophysin (UTR; syp_utr#3)	GAG CCC GCT GTG TTT AAG CCA CAC CCC TCC TAG AAC CAC TCT CTC TGG TCA CTT A
synaptotagmin (coding sequence; syt#1)	CAT AAA CTT CTG CTT CAG CTT GGA AAA GGC ATC TTC CTT CCC TTC CCC AGG ACT G
synaptotagmin (coding sequence; syt#2)	CTG GAG ATC ACG CCA CTC CTC GGT CAC ATG GCC AAA ATC CAC GGT GTT CAT AGG A
synaptotagmin (coding sequence; syt#3)	GCC CCA GTG CTG TTG TAA CCA ACG AAG ACT TTG CCG ATG GCG TCG TTC TTG CCA A
synaptotagmin (UTR; syt_utr#1)	CAA AGT CTT CCG ATC TGA CTG CGG ATG TTG GTT GCT CAA GCG CTT TCA AGT CTT C
synaptotagmin (UTR; syt_utr#2)	CTC GGA ATC TTT CTT CAA TCT TAA TGA GAC GTT CTG GTG GCG CTC TGG GGA TGG C
synaptotagmin (UTR; syt_utr#3)	ACA GAT ACT GGC TAA AGA GCA CTA TGT GGG CAG ATG CAG AAA GGC TTC GTT TTC C
synaptobrevin (coding sequence; syb#1)	AGA TGA TCA TCA TCT TGA GGT TTT TCC ACC AGT ATT TGC GCT TGA GCT TGG CTG C
synaptobrevin (coding sequence; syb#2)	CAT CCA CCT GGG CCT GGG TCT GCT GCA GTC TCC TGT TAC TGG TAA GAT TTG GAG G
synaptobrevin (coding sequence; syb#3)	CGA TCA TCC AGT TCC GAT AGC TTC TGG TCC CGC TCC AGG ACC TTG TCC ACA TTC A
synaptobrevin (UTR; syb_utr#1)	TAA CAG CTG GCT ATT TAC AGG GGG CAC ACA CAC GGA CAC ACA CAC ACA CGG ATC C
synaptobrevin (UTR; syb_utr#2)	GGG GTT TGC TCT GTT TGG GGA GGG TCT GGA ATT GTA CAG GGA AGA TAG GGG AAG G
synaptobrevin (UTR; syb_utr#3)	GAG GCT CCC AAG GGA TAC AAA GAT GCA ACC TAT GGA AGC CTA GAC AGG TGG GGT G
random control probes (rnd#1)	TTA AAC ACA ACG ACG ACC GGG AAC AAT CAT TAT GGC ACG CGG AGC AAT GGC TAA C
random control probes (rnd#2)	AGA CGC AAC AAG ATT ACG TAC GCG AAC GAA GTA CGC ACG TCA GGT TCA AAT CGC A
random control probes (rnd#3)	GAC CTA ATA CGT ACC ACC CGA AGG GTA CGT GTA AAG ATA GGC CGA CTA CGA AAC A

4.6.2. Immunostaining of cells (after FISH)

After the last rinse with 1x SSC during the FISH procedure, the cells were fixed with 4% paraformaldehyde (PFA) and quenched again, as described previously. The cells were then permeabilized with 0.1% Triton-X (Merck) in PBS for 5 minutes. Primary and secondary antibodies were diluted 1:250 and 1:1000, respectively, in 1.5% bovine serum albumin (BSA) and 0.1% Triton-X in PBS. Guinea pig anti-synaptophysin and mouse anti-MAP2 antibodies were incubated prior to fluorescently labeled secondary antibodies. Each antibody incubation of 1 hour was followed by extensive washings with PBS. The cells were then embedded in Mowiol and stored as described above.

4.7. Immunostaining of CSF

4.7.1. Synthetic Aβ samples

$A\beta_{4-38}$ and $A\beta_{1-42}$ peptides were dissolved in 1,1,1,3,3,3-hexafluoro-2-propanol (HFIP, PSL), flash-frozen in liquid nitrogen, and then lyophilized to completely remove the solvent. Lyophilized Aβ peptides were re-dissolved in 100 mM NaOH at a concentration of 2 mg/ml, aliquoted, flash-frozen with liquid nitrogen, and stored at -80ºC until use. Size-exclusion chromatography (SEC) was performed using a Superose 6 10/300 column (GE Healthcare) connected to an ÄKTApurifier^{TM} 10 UPC 900 system (GE Healthcare). The samples were prepared in phosphate buffer (50 mM, pH 7.4) with 50 mM NaCl, at a peptide concentration of 0.5 mg/µl and then incubated at 37ºC for 24 h, without further promotion of aggregation by agitation. After a short centrifugation step, 250 µl of peptide solution was loaded onto the column at a flow rate of 0.5 ml/min. The peptide elution was monitored by UV absorbance at 215 and 265 nm. The SEC peaks were calibrated and corresponding stoichiometries were calculated as previously published (Paivio et al., 2004). $A\beta_{4-38}$ was used to isolate stable LMW (dimers/trimers) and $A\beta_{1-42}$ for HMW aggregates (Bouter et al., 2013).

4.7.2. Human subjects

Cerebrospinal fluid (CSF) was collected and stored at one clinical center according to one standard operation procedure (SOP) to minimize storage and sample handling artifacts. CSF was obtained from the Biobank at the Department of Psychiatry (University Medical Center). Patients with Alzheimer's Disease (AD) and mild cognitive impairment (MCI) were clinically phenotyped by neuropsychological testing (CERAD Plus test battery as the minimum assessment), neurological examination, MRI, and CSF diagnostics by the Memory Clinic's specialized physicians (University Medical Center). AD diagnosis was based on the criteria of the National Institute of Neurological and Communicative Disorders and Stroke and the Alzheimer's Disease and Related Disorders Association (NINCDS-ADRDA). Patients with preserved activities of daily living but showing a combination of memory complaints plus a performance of 1-1.5 standard deviations below the age norm on at least one cognitive domain of the CERAD Plus test battery were considered as MCIs (Winblad et al., 2004). Control samples were provided by the Departments of Psychiatry and Neurology (University Medical Center) including patients with schizophrenia, bipolar disorder, depression, multiple sclerosis, and headache. Patients of the control group with memory deficits (e.g. due to negative symptoms caused by schizophrenia) were neuropsychologically assessed and patients with dementia or neurodegenerative diseases were excluded from controls. Biosampling was conducted according to the Declaration of Helsinki and was approved by the ethics committee of the University Medical Center Göttingen (approval number 2/5/09) and all patients gave informed written consent. For detailed information, please refer to Tables B-E.

4.7.3. CSF samples

CSF samples were collected at the memory clinic and the Department of Psychiatry (University Medical Center) starting in 2010, following identical SOPs. In short, CSF was obtained between 9 a.m. and 1 p.m. and centrifuged for 10 minutes at 2000x g and room temperature within 20 minutes after the lumbar puncture. The supernatant was then aliquoted, flash frozen, and stored at -80ºC. CSF samples containing blood contamination were excluded.

Six post-mortem CSF samples from confirmed AD patients were obtained from the Tissue Bank, Fundación CIEN (Instituto de Salud Carlos III). Rapid brain autopsies were performed according to the brain bank protocol (Martinez-Martin et al., 2010). CSF (10-15 ml on average) was obtained during autopsy by puncture of the IIIrd ventricle through its floor, immediately behind the optic chiasm before removal of the brain. The CSF was assessed regarding to its color and macroscopic

properties, as well as its pH was measured. The CSF samples were subsequently centrifuged for 8 minutes at 1300x g and 4ºC. 0.5-1 ml aliquots of the supernatant were prepared and stored as stated above.

Enzyme-linked immunosorbent assay (ELISA) measurements of these samples were performed commercially (Universitätsklinikum Tübingen) according established methods. The quantities of $A\beta_{1-42}$ and tau were determined and are shown in Tables B-E.

(D) Table | Patient information and CSF properties from controls.

ID	**diagnosis**	**sex**	age **[years]**	Abeta **[pg/ml]**	tau **[pg/ml]**	**$F_{A\beta}$**
63	fragile X	m	20	576	91	45.616
67	polyneuropathy	f	64	669	175	3.794
78	multiple sclerosis	f	60	240	979	56.714
92	schizophrenia	m	59	440	197	63.227
101	schizophrenia	m	49	469	190	3.594
106	multiple sclerosis	m	57	781	290	37.753
120	severe depression	f	57	622	347	55.442
126	schizophrenia	m	42	1265	365	54.643
130	schizophrenia	m	19	790	202	47.392
131	severe depression	m	60	632	339	35.724
132	schizophrenia	f	34	518	154	5.028
135	severe depression	m	48	809	217	27.836
138	anxiety, depression	f	48	621	214	42.764
140	depression	f	63	828	613	40.098
151	schizophrenia	f	42	654	150	35.071
161	severe depression	f	24	182	788	49.997
166	severe depression	m	48	452	97	41.773
167	schizophrenia	m	20	690	136	46.549
172	schizophrenia	f	55	915	226	50.501
173	schizophrenia	m	23	914	287	48.022
177	severe depression	m	54	1006	296	44.856

(E) Table | Patient information and CSF properties from AD patients.

ID	**sex**	**age [years]**	**MMSE**	**Abeta [pg/ml]**	**tau [pg/ml]**	**$F_{A\beta}$**	**$F_{A\beta,\ tau}$**
4	m	70	23	423	136	2.747	12.933
6	f	69	9	275	927	2.585	12.576
16	m	79	26	170	424	36.484	16.928
22	m	58	17	613	109	29.683	14.698
47	m	64	27	334	422	42.355	16.676
57	m	73	22	269	253	15.997	0.9657

60	f	78	21	223	346	37.072	14.241
61	f	59	17	229	832	16.045	10.675
65	f	83	6	260	342	12.268	0.9709
69	m	72	22	215	477	10.848	0.8931
73	m	74	22	220	368	30.845	16.877
76	m	63	25	311	425	28.863	15.778
84	f	74	27	285	327	30.735	11.852
89	f	54	20	135	725	11.943	
98	f	76	24	489	422	37.647	16.408
107	f	78	22	224	542	37.069	16.408
111	m	62	27	316	828	33.758	15.455
112	f	72	25	12	140	49.645	19.203
114	f	69	26	439	323	31.976	16.496
115	m	71	28	307	424	24.652	22.336
116	f	82	23	402	173	28.853	
119	f	71	22	130	923	29.686	15.421
123	f	75	23	443	832	46.084	14.502
124	f	72	23	155	1033	46.037	13.553
141	f	57	28	638	616	15.024	
144	m	73	27	368	652	48.801	
145	m	79	28	917	374	48.196	
148	f	75	27	153	272	21.772	
159	m	67	21	567	152	51.414	
163	m	77	25	396	236	50.351	

(F) Table | Patient information and CSF properties from AD cases confirmed by autopsy.

ID	sex	age [years]	$F_{A\beta}$	$F_{A\beta,\ tau}$
48	f	84	0.9168	0.8542
190	m	94	0.6843	22.187
213	f	91	1.582	14.741
1742	f	82	12.355	15.842
1749	f	67	16.383	1.258
1752	m	65	12.832	20.438

(G) Table | Patient information and CSF properties from mild cognitive impaired (MCI). The asterisks indicate the patients that were diagnosed with full AD during the study.

ID	sex	age [years]	MMSE	Abeta [pg/ml]	tau [pg/ml]	$F_{Aβ}$	$F_{Aβ, tau}$
59*	f	78	29	160	410	29.371	12.855
72	m	65	28	327	617	24.176	12.979
74	m	70	27	254	286	29.023	1.448
80	m	54	26			23.497	11.403
81	m	71	25	336	1147	1.349	0.9682
83	m	70	27	474	188	64.559	23.248
86	m	59	30	286	178	58.355	21.622
91	m	71	30	561	327	49.994	17.832
94	f	67	28	837	150	36.526	14.384
95*	f	74	28	235		45.476	15.715
164	m	64	29	881	424	45.028	

4.7.4. Immunostaining

Freshly prepared PLL-coated coverslips were briefly washed with PBS and CSF samples were immediately added for 30 minutes in a humidifying chamber. The CSF was then fixed with 4% PFA for 25 minutes and quenched with 0.1 M NH_4Cl for 10 minutes. Unless otherwise stated, the samples were blocked for 30 minutes with 5% BSA and 5% peptone in PBS. The CSF was immunostained with the respective primary antibody in blocking solution for one hour. Excess antibodies were removed by three washings with PBS for 5 minutes each before 1 hour incubation with secondary Fab fragments coupled to Atto647N fluorophores in blocking solution. The coverslips were subsequently rinsed three times with high salt PBS and twice with PBS for 5 minutes each. The coverslips were embedded and stores as described above.

4.8. Epifluorescence imaging

Wide-field fluorescence images were taken at an Olympus IX71 microscope (Olympus) equipped with an 100x oil TIRFM objective (1.45 numerical aperture, NA; Olympus) and an F-View II charge-coupled device (CCD) camera (1376 pixels x 1032 pixels with a pixel size of 6.45 µm x 6.45 µm). All filters were purchased from Chroma and are listed in Table H.

(H) Table | List of filter cubes for epifluorescence imaging.

filter	excitation	beamsplitter	emission
DAPI	350/50 D	400 DCLP	460/50 D
FITC	480/40 HQ	505 LP Q	527/30 HQ
TRITC	545/30 HQ	570 LP Q	610/75 HQ
Cy5	620/60 HQ	660 LP Q	700/75 HQ

4.9. Confocal and STED imaging

Confocal and STED images were taken at a Leica TCS SP5 STED microscope (Leica) with a 100x HCX PL APO CS oil objective (1.4 NA; Leica). A 635 nm pulsed diode laser (Leica) was used for excitation. To create the super-imposed donut for depletion, a Spectra-Physics MaiTai multiphoton laser at 750 nm (pulsed at 80 MHz, ~1.3 W output power with the 100x objective, Titanium Sapphire; Newport Spectra-Physics) was used. For multichannel confocal imaging, the following settings were used: Argon laser at 488 nm for GFP, Cy2, or autofluorescence; Helium-Neon lasers at 594 nm or 633 nm for Cy3 or Atto647N, respectively. Images were taken sequentially line by line at a scanning frequency of 1000 Hz with 16 or 32 times for confocal and 96 times line averaging for STED mode. Fluorescence was detected by photomultiplier tubes (PMT) for confocal or by an avalanche photodiode (APD) for STED images using laser intensities with the best signal-to-noise ratio for each experiment. The STED resolution ~50 nm.

4.10. Image analysis

All analyses were performed using custom-written macros (mostly developed by Silvio O. Rizzoli) for MatLab (Mathworks). For better visibility, STED images were deconvolved with Huygens Essential 3.3 (Scientific Volume Imaging) using a classical maximum likelihood estimation (CMLE) algorithm.

4.11. Statistics

All data is presented as mean ± SEM, unless stated otherwise. SigmaPlot (Mathworks) was used for student's t-test (unpaired) and the p-values were obtained. Statistical significance is denoted as non-

significant (n.s.) when $p > 0.05$; as * when $P < 0.05$; as ** when $p < 0.01$, and as ***, when $P < 0.001$.

5. Bibliography

(2005) Springer Series on Fluorescence: Springer.

Abbe E (1873) Beiträge zur Theorie des Mikroskops und der mikroskopischen Wahrnehmung. Archiv f mikrosk Anatomie 9:413-418.

Alberts BJ, Alexander; Lewis, Julian; Raff, Martin; Roberts, Keith; Walter, Peter (2014) Molecular Biology of the Cell. New York: Garland Science.

Alzheimer A (1907) Über eine eigenartige Erkrankung der Hirnrinde. Allgemine Zeitschrift für Psychiatrie und physisch-gerichtliche Medizin 146-148.

Andreasen N, Blennow K (2005) CSF biomarkers for mild cognitive impairment and early Alzheimer's disease. Clinical neurology and neurosurgery 107:165-173.

Baker HvL, Anton (1739) An Account of Mr. Leeuwenhoek's Microscopes; by Mr. Henry Baker, F.R.S. Phil Trans 503-519.

Bartel D (2004) MicroRNA: genomics, biogenesis, mechanism, and function. Cell 116:281-297.

Betzig EP, GH; Sougrat, R; Lindwasser, OW; Olenych, S; Bonifacino, JS; Davidson, MW; Lippincott-Schwartz, J; Hess, HF (2006) Imaging intracellular fluorescent proteins at nanometer resolution. Science 1642-1645.

Blessed GT, BE; Roth, Martin (1968) The association between quantitative measures of dementia and of senile change in the cerebral gray matter of elderly subjects. Brit J Psychiatry 797-811.

Bouter Y, Dietrich K, Wittnam JL, Rezaei-Ghaleh N, Pillot T, Papot-Couturier S, Lefebvre T, Sprenger F, Wirths O, Zweckstetter M, Bayer TA (2013) N-truncated amyloid beta (Abeta) 4-42 forms stable aggregates and induces acute and long-lasting behavioral deficits. Acta neuropathologica 126:189-205.

Cicognola C, Chiasserini D, Parnetti L (2015) Preanalytical Confounding Factors in the Analysis of Cerebrospinal Fluid Biomarkers for Alzheimer's Disease: The Issue of Diurnal Variation. Front Neurol 6:143.

Dickson DK-R, H; Liu, WK; Davies, P; Crowe, A; Yen, SH (1992) Immunocytochemistry of neurofibrillary tangles with antibodies to subregions of tau protein: identification of hidden and cleaved tau epitopes and a new phosphorylation site. Acta neuropathologica 84:596-605.

Duce JA, Tsatsanis A, Cater MA, James SA, Robb E, Wikhe K, Leong SL, Perez K, Johanssen T, Greenough MA, Cho HH, Galatis D, Moir RD, Masters CL, McLean C, Tanzi RE, Cappai R, Barnham KJ, Ciccotosto GD, Rogers JT, Bush AI (2010) Iron-export ferroxidase activity of beta-amyloid precursor protein is inhibited by zinc in Alzheimer's disease. Cell 142:857-867.

Ebbesen KK, Kjems J, Hansen TB (2015) Circular RNAs: Identification, biogenesis and function. Biochim Biophys Acta.

Einstein A (1916) Strahlungs-Emission und -Absorption nach der Quantentheorie. Deutsche Physikalische Gesellschaft, Verhandlungen 318-323.

Erni RR, MD; Kisielowski, C; Dahmen, U (2009) Atomic-resolution imaging with a sub-50-pm electron probe. Phys Rev Lett 102.

Esparza TJ, Zhao H, Cirrito JR, Cairns NJ, Bateman RJ, Holtzman DM, Brody DL (2013) Amyloid-beta oligomerization in Alzheimer dementia versus high-pathology controls. Annals of neurology 73:104-119.

Fourier A, Portelius E, Zetterberg H, Blennow K, Quadrio I, Perret-Liaudet A (2015) Pre-analytical and analytical factors influencing Alzheimer's disease cerebrospinal fluid biomarker variability. Clin Chim Acta 449:9-15.

Fukumoto H, Tokuda T, Kasai T, Ishigami N, Hidaka H, Kondo M, Allsop D, Nakagawa M (2010) High-molecular-weight beta-amyloid oligomers are elevated in cerebrospinal fluid of Alzheimer patients. FASEB J 24:2716-2726.

Georganopoulou DG, Chang L, Nam JM, Thaxton CS, Mufson EJ, Klein WL, Mirkin CA (2005) Nanoparticle-based detection in cerebral spinal fluid of a soluble pathogenic biomarker for Alzheimer's disease. Proceedings of the National Academy of Sciences of the United States of America 102:2273-2276.

Glenner GG, Wong CW (1984) Alzheimer's disease: initial report of the purification and characterization of a novel cerebrovascular amyloid protein. Biochemical and biophysical research communications 425:534-539.

Golgi C (1873) Sulla struttura della sostanza grigia del cervello. Gazz Med Ital Lomb 244-246.

Heumann R, Kachel V, Thoenen H (1983) Relationship between NGF-mediated volume increase and "priming effect" in fast and slow reacting clones of PC12 pheochromocytoma cells. Role of cAMP. Experimental cell research 145:179-190.

Hoagland MK, EB; Zamecnik, PC (1956) Enzymatic carboxyl activation of amino acids. The Journal of biological chemistry 218:345-358.

Hooke R (1665) Micrographia: or some physiological descriptions of minute bodies made by magnifying glasses: with observations and iquiries thereupon. Courier Corporation.

Hulstaert F, Blennow K, Ivanoiu A, Schoonderwaldt HC, Riemenschneider M, Deyn PPD, Bancher C, Cras P, Wiltfang J, Mehta PD, Iqbal K, Pottel H, Vanmechelen E, Vanderstichele H (1999) Improved discrimination of AD patients using -amyloid(1-42) and tau levels in CSF. Neurology 52:1555-1555.

Irizarry M (2004) Biomarkers of Alzheimer disease in plasma. NeuroRx 1:226-234.

Jacob FM, Jacques (1961) Genetic Regulatory Mechanisms in the Synthesis of Proteins. Journal of molecular biology 318-356.

Kapranov P, Cheng J, Dike S, Nix DA, Duttagupta R, Willingham AT, Stadler PF, Hertel J, Hackermuller J, Hofacker IL, Bell I, Cheung E, Drenkow J, Dumais E, Patel S, Helt G,

Ganesh M, Ghosh S, Piccolboni A, Sementchenko V, Tammana H, Gingeras TR (2007) RNA maps reveal new RNA classes and a possible function for pervasive transcription. Science 316:1484-1488.

Kayed R, Head E, Sarsoza F, Saing T, Cotman CW, Necula M, Margol L, Wu J, Breydo L, Thompson JL, Rasool S, Gurlo T, Butler P, Glabe CG (2007) Fibril specific, conformation dependent antibodies recognize a generic epitope common to amyloid fibrils and fibrillar oligomers that is absent in prefibrillar oligomers. Molecular neurodegeneration 2:18.

Lewis MA, Steel KP (2010) MicroRNAs in mouse development and disease. Semin Cell Dev Biol 21:774-780.

Maddalena AS, Papassotiropoulos A, Gonzalez-Agosti C, Signorell A, Hegi T, Pasch T, Nitsch RM, Hock C (2004) Cerebrospinal fluid profile of amyloid beta peptides in patients with Alzheimer's disease determined by protein biochip technology. Neurodegener Dis 1:231-235.

Martinez-Martin P, Avila J, Investigators ADRU (2010) Alzheimer Center Reina Sofia Foundation: fighting the disease and providing overall solutions. Journal of Alzheimer's disease : JAD 21:337-348.

Massey M, Wu M, Conroy EM, Algar WR (2015) Mind your P's and Q's: the coming of age of semiconducting polymer dots and semiconductor quantum dots in biological applications. Curr Opin Biotechnol 34:30-40.

Mayeux R, Honig LS, Tang MX, Manly J, Stern Y, Schupf N, Mehta PD (2003) Plasma A 40 and A 42 and Alzheimer's disease: Relation to age, mortality, and risk. Neurology 61:1185-1190.

McKhann GM, Knopman DS, Chertkow H, Hyman BT, Jack CR, Jr., Kawas CH, Klunk WE, Koroshetz WJ, Manly JJ, Mayeux R, Mohs RC, Morris JC, Rossor MN, Scheltens P, Carrillo MC, Thies B, Weintraub S, Phelps CH (2011) The diagnosis of dementia due to Alzheimer's disease: recommendations from the National Institute on Aging-Alzheimer's Association workgroups on diagnostic guidelines for Alzheimer's disease. Alzheimer's & dementia : the journal of the Alzheimer's Association 7:263-269.

Moerner WE (2006) Single-molecule mountains yield nanoscale cell images. Nature methods 3:781-782.

Morris M, Maeda S, Vossel K, Mucke L (2011) The many faces of tau. Neuron 70:410-426.

Motter RV-P, C; Kholodenko, D; Barbour, R; Johnson-Wood, K; Galasko, D; Chang, L; Miller, B; Clark, C; Green, R; Olson, D; Southwick, P; Wolfert, R; Munroe, B; Liebergurg, I; Seubert, P; Schenk, D (1995) Reduction of beta-amyloid peptide42 in the cerebrospinal fluid of patients with Alzheimer's disease. Annals of neurology 38:643-648.

Paivio A, Jarvet J, Graslund A, Lannfelt L, Westlind-Danielsson A (2004) Unique physicochemical profile of beta-amyloid peptide variant Abeta1-40E22G protofibrils: conceivable neuropathogen in arctic mutant carriers. Journal of molecular biology 339:145-159.

Pirttilä T, Kim K, Mehta PD, Frey H, Wisniewski H (1994) Soluble amyloid beta-protein in the cerebrospinal fluid from patients with Alzheimer's disease, vascular dementia and controls. J Neurol Sci 127:90-95.

Priller C, Bauer T, Mitteregger G, Krebs B, Kretzschmar HA, Herms J (2006) Synapse formation and function is modulated by the amyloid precursor protein. The Journal of neuroscience : the official journal of the Society for Neuroscience 26:7212-7221.

Ramón y Cajal S (1917) Recuerdos de mi vida. Madrid: Moya.

Savage MJ, Kalinina J, Wolfe A, Tugusheva K, Korn R, Cash-Mason T, Maxwell JW, Hatcher NG, Haugabook SJ, Wu G, Howell BJ, Renger JJ, Shughrue PJ, McCampbell A (2014) A sensitive abeta oligomer assay discriminates Alzheimer's and aged control cerebrospinal fluid. The Journal of neuroscience : the official journal of the Society for Neuroscience 34:2884-2897.

Scheuner D, Eckman C, Jensen M, Song X, Citron M, Suzuki N, Bird T, Hardy J, Hutton M, Kukull W, Larson E, Levy-Lahad E, Viitanen M, Peskind E, Poorkaj P, Schellenberg G, Tanzi R, Wasco W, Lannfelt L, Selkoe D, Younkin S (1996) Secreted amyloid beta-protein similar to that in the senile plaques of Alzheimer's disease is increased in vivo by the presenilin 1 and 2 and APP mutations linked to familial Alzheimer's disease. Nat Med 2:864-870.

Schoonenboom NS, Mulder C, Vanderstichele H, Van Elk EJ, Kok A, Van Kamp GJ, Scheltens P, Blankenstein MA (2005) Effects of processing and storage conditions on amyloid beta (1-42) and tau concentrations in cerebrospinal fluid: implications for use in clinical practice. Clin Chem 51:189-195.

Shtengel G, Wang Y, Zhang Z, Goh WI, Hess HF, Kanchanawong P (2014) Imaging cellular ultrastructure by PALM, iPALM, and correlative iPALM-EM. Methods Cell Biol 123:273-294.

Tapia JC, Kasthuri N, Hayworth KJ, Schalek R, Lichtman JW, Smith SJ, Buchanan J (2012) High-contrast en bloc staining of neuronal tissue for field emission scanning electron microscopy. Nature protocols 7:193-206.

Terry RD, Masliah E, Salmon DP, Butters N, DeTeresa R, Hill R, Hansen LA, Katzman R (1991) Physical basis of cognitive alterations in Alzheimerr's disease: synapse loss is the major correlate of cognitive impairment. Annals of neurology 30:572-580.

Toomre D, Bewersdorf J (2010) A new wave of cellular imaging. Annual review of cell and developmental biology 26:285-314.

Turner PR, O'Connor K, Tate WP, Abraham WC (2003) Roles of amyloid precursor protein and its fragments in regulating neural activity, plasticity and memory. Progress in Neurobiology 70:1-32.

van Oijen M, Hofman A, Soares HD, Koudstaal PJ, Breteler MMB (2006) Plasma Aβ1–40 and Aβ1–42 and the risk of dementia: a prospective case-cohort study. The Lancet Neurology 5:655-660.

Viola KL, Klein WL (2015) Amyloid beta oligomers in Alzheimer's disease pathogenesis, treatment, and diagnosis. Acta neuropathologica 129:183-206.

Willig KI, Rizzoli SO, Westphal V, Jahn R, Hell SW (2006) STED microscopy reveals that synaptotagmin remains clustered after synaptic vesicle exocytosis. Nature 440:935-939.

Winblad B, Palmer K, Kivipelto M, Jelic V, Fratiglioni L, Wahlund L-O, Nordberg A, Bäckman L, Albert M, Almkvist O, Arai H, Basun H, Blennow K, de Leon M, Decarli C, Erkinjuntti T,

van Duijn C, Visser P, Petersen RC (2004) Mild cognitive impariment - beyond controversies, towards a consensus: report of the International Working Group on Mild Cognitive Impairment. Journal of Internal Medicine 256:240-246.

Wirths O, Bethge T, Marcello A, Harmeier A, Jawhar S, Lucassen PJ, Multhaup G, Brody DL, Esparza T, Ingelsson M, Kalimo H, Lannfelt L, Bayer TA (2010) Pyroglutamate Abeta pathology in APP/PS1KI mice, sporadic and familial Alzheimer's disease cases. Journal of neural transmission 117:85-96.

Zanetti-Domingues LC, Tynan CJ, Rolfe DJ, Clarke DT, Martin-Fernandez M (2013) Hydrophobic fluorescent probes introduce artifacts into single molecule tracking experiments due to non-specific binding. PloS one 8:e74200.

Zetterberg H, Blennow K (2013) Cerebrospinal fluid biomarkers for Alzheimer's disease: more to come? Journal of Alzheimer's disease : JAD 33 Suppl 1:S361-369.

Zhang WI (2011) Investigation of mRNA dynamics and protein synthesis upon neuronal activity. vol. Master Göttingen: University of Göttingen.

Zimmermann R, Lelental N, Ganslandt O, Maler JM, Kornhuber J, Lewczuk P (2011) Preanalytical sample handling and sample stability testing for the neurochemical dementia diagnostics. Journal of Alzheimer's disease : JAD 25:739-745.